OCTA

Integrated simulation system for soft materials

APPLICATION REPORT

AMUSE

Nagoya University, Doi Project
Research and Development of the Platform
for Designing High Functional Materials

Computer Aided Materials Design Joint Research
Japan Chemical Innovation Institute (JCII)

FEB. 22 2002

Authors of the Report

Chapter 1	Hiroyasu Tasaki
Chapter 2	Tatsuya Shoji, Hiroya Kodama, Takeshi Aoyagi
Chapter 3	Masahiro Noda
Chapter 4	Katsuyuki Yokomizo, Takeshi Aoyagi
Chapter 5	Hiroyasu Tasaki
Appendix A	Tatsuya Shoji, Masahiro Noda, Katsuyuki Yokomizo

AMUSE project members

Takeshi Aoyagi
Hiroya Kodama
Makoto Sasaki
Tatsuya Shoji
Hiroyasu Tasaki
Masahiro Noda
Takashi Honda
Katsuyuki Yokomizo
Yuichi Masubuchi

Acknowledgment

This work is supported by the national project, which has been entrusted to the Japan Chemical Innovation Institute (JCII) by the New Energy and Industrial Technology Development Organization (NEDO) under METI's Program for the Scientific Technology Development for Industries that Creates New Industries.

Contents

List of Figures

List of Tables

Chapter 1

Introduction

OCTA is developed to be a prototype system for computer aided material design. OCTA is aiming at the simulation technology brought by the collaboration of various simulation programs. OCTA consists of four simulation engines each dealing with certain characteristic aspect of the material. To explore the possibility of OCTA we conducted a project **AMUSE**(*Advanced Materials design Using Simulation Engines*) in which a certain test material is studied by utilizing the collaboration of engines.

As the test material, we chose Polypropylene(PP) materials which consists of PP and elastomers(EPR, SEBS etc.). An important objective of the PP material design is to make stiff and tough. For this objective, the following properties must be controlled.

* Orientation of the polypropylene crystallite.
* Tie molecules related to the molecular weight and tacticity of polypropylene.
* Morphology of a polypropylene/elastomer blend.
* Conformation at a polypropylene/elastomer interface.

Thus we paid attention to the PP crystal, the morphology in the blend of PP and elastomers and the interface between them. The outline of AMUSE is shown in Fig.1.1.

1. Study of mechanical properties of semicrystalline polymer.
   A method of generating the initial semicrystalline lamella structure is developed. By zooming from the structure calculated by SUSHI, to COGNAC, we propose the forecasting model of elasticity of the polypropylene crystal in consideration of the amorphous layer. The elastic modulus calculated by COGNAC can be used in MUFFIN as a material parameter(a zooming from COGNAC to MUFFIN.).

2. Prediction of bulk elasticity of polypropylene/elastomer blends.
   MUFFIN can calculate an elastic modulus of the material having some morphology. SUSHI can simulate the morphology of polypropylene/elastomer blend system. Therefore, elastic modulus of bulk material can be predicted by zooming from SUSHI to MUFFIN.

3. Prediction of interfacial strength of polypropylene/elastomer blends.
   A method of generating the initial structure of polymer chain at an interface is developed. By zooming from SUSHI to COGNAC, we study the interfacial properties of polypropylene/elastomer blend system influenced by the interfacial thickness and the conformation at an interface.
   Obtained interfacial strength may be used to predict the mechanical properties of bulk material reflecting the physical properties at an interface(future work).

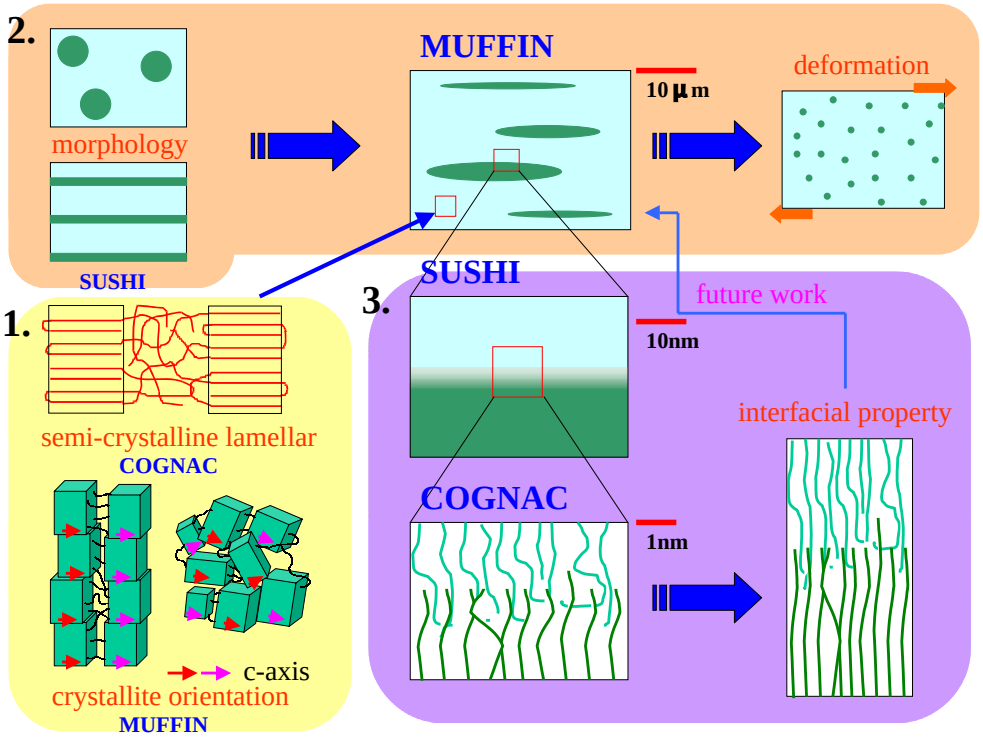

Figure 1.1: Outline of AMUSE. 1. Calculation of elastic modulus of the semicrystalline lamella structure obtained by zooming. Influence of crystallite orientation exerted on bulk elasticity is also examined. 2. Prediction of bulk morphology and elastic modulus by zooming from SUSHI to MUFFIN. 3. Study of interfacial strength influenced by chain conformation at an interface obtained by zooming from SUSHI to COGNAC.

Chapter 2

Lamella structures of semi-crystalline polymers

2.1 Introduction

Semi-crystalline polymers generally form lamella structures of alternating crystalline and amorphous phases. Typical thickness of these phases are 100-500Å for crystalline phase and 50-200Å for amorphous phase. Chains in amorphous portion can be classified into (i) loop-, (ii) bridge-, (iii) tail- and (iv) free-chains. It has been known that in order for amorphous phases to be occupied by amorphous chains with an adequate density, tight loop chains have to dominate the chain population distribution. It is considered that the chain structures in the amorphous phase is related to mechanical properties of such materials containing semi-crystalline polymers. Computational approach to this problem should play an important role because of the difficulties in experimental access to the chain structures.

In the AMUSE, it is planned to perform a unique computational analysis for the elastic modulus of lamella structures of semi-crystalline polyolefin materials, where COGNAC and SUSHI are used cooperatively. Furthermore, passing the results to MUFFIN, it would be enabled to simulate the mechanical properties of larger scale structures including phase separated domains.

Here we consider the limiting case that the polymer chains are infinitely long. Then, the only possible type of chains in amorphous phases are either loop- or bridge-chains. In the following sections, results for chain populations obtained by using SUSHI calculation (even analytic expression is found in this limit) are given. Next, we show that the results of SUSHI can be used as a guide to generate the initial chain configuration of semi-crystalline lamella structures for COGNAC simulation by "lamella generator". Then we demonstrate the COGNAC simulation for deformations of the lamella structures. The resulting chain structures at large strains as well as the elastic modulus are shown[1].

2.2 Analysis of chain conformation in amorphous phase

2.2.1 Mean field calculation

In the beginning of 1980s, the population of loop- and bridge- chains in amorphous phases are analyzed in terms of random walk model [2, 3]. In the present work, we solved a set of self-consistent field equations governing the chain structures in the amorphous phases. A melt condition ensuring the constant chain density within the amorphous phases is imposed in a self-consistent way.

We set the model as the following. Let us consider two walls separated by distance d and the amorphous chains are distributed between the walls with a constant density. The problem is to derive the chain length distribution when the chain ends are attached either of the two walls (Fig. 2.1). Note that no free ends exist since the infinite chain length is assumed.

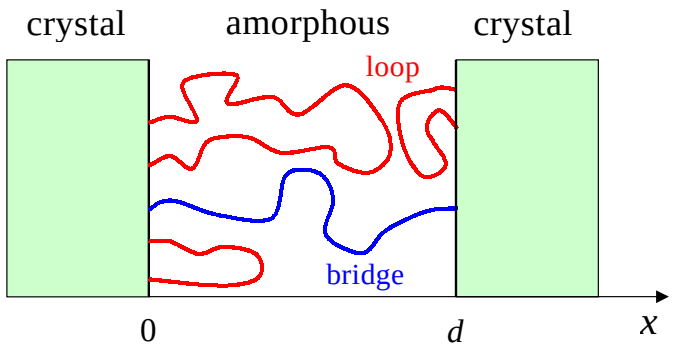

Figure 2.1: infinite-chain-length model of semi-crystalline polymers.

Let us consider an amorphous chain having the length s and starting on the left hand side wall. The end distribution, $\mathcal{Q}^{(L)}(s,x)$ of the chain is given by the diffusion equation,

$$\frac{\partial}{\partial s}\mathcal{Q}^{(L)}(s,x) = \frac{b^2}{6}\nabla^2\mathcal{Q}^{(L)}(s,x) - V(x)\,\mathcal{Q}^{(L)}(s,x) \tag{2.1}$$

with the initial condition,

$$\mathcal{Q}^{(L)}(0,x) = \delta(x-\varepsilon) \tag{2.2}$$

Here, ε is a small constant and we eventually take a limit of $\varepsilon \to 0$. $V(x)$ is a Lagrange multiplier for the local melt condition. The end distribution of the chain starting on the right hand side wall can be obtained in the same way. Let us denote the number of the left-hand-side and right-hand-side loop-chains per area as $n_\ell^{(L)}(m)$ and $n_\ell^{(R)}(m)$, respectively. The number of bridge-chains per area is also denoted as $n_b(m)$. When the chain distribution $\left(\{n_\ell^{(L)}(m)\},\{n_\ell^{(R)}(m)\},\{n_b(m)\}\right)$ is given under the condition

$$\sum_m mb^3\{n_\ell^{(L)}(m) + n_\ell^{(R)}(m) + n_b(m)\} = d, \tag{2.3}$$

the volume fraction $\phi_\ell^{(L)}(s,x \mid m)$ of the s-th segment of the left-hand-side loop chains with the length m becomes

$$\phi_\ell^{(L)}(s,x \mid m) = C_\ell^{(L)}(m)\mathcal{Q}^{(L)}(s,x)\mathcal{Q}^{(L)}(m-s,x), \tag{2.4}$$

where $C_\ell^{(L)}(m)$ is the normalization constant given by

$$C_\ell^{(L)}(m) = \frac{n_\ell^{(L)}(m)}{\mathcal{Q}^{(L)}(m,0)}. \tag{2.5}$$

The same is true for the volume fractions of the loop-chain on the opposite side and the bridge-chain. The problem is to find the distribution $\left(\{n_\ell^{(L)}(m)\},\{n_\ell^{(R)}(m)\},\{n_b(m)\}\right)$ which minimize the free energy. This

can be done by solving the grand canonical ensemble setting the chemical potential of the chain proportional to m. Hence, we just replace the right-hand-side of eq.(2.5) by a constant C which is independent of m. Below, we denote the total loop distribution as $n_\ell(m) = n_\ell^{(L)}(m) + n_\ell^{(R)}(m)$.

Using the above model, we solved the distributions of the loop- and bridge-chains for $d = 5, 6, 7, 8$ and plotted in fig.2.2, fig.2.3, respectively. The distribution of the loop-chains is dominated by the tight loop

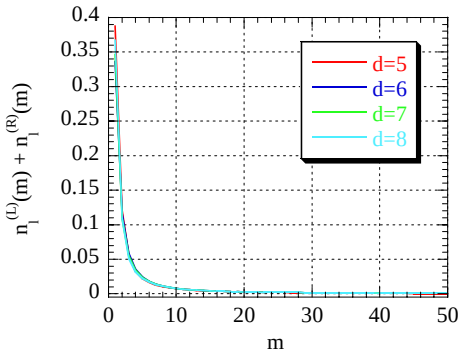

Figure 2.2: The number of loop-chains with the length m per unit area in the amorphous phase.

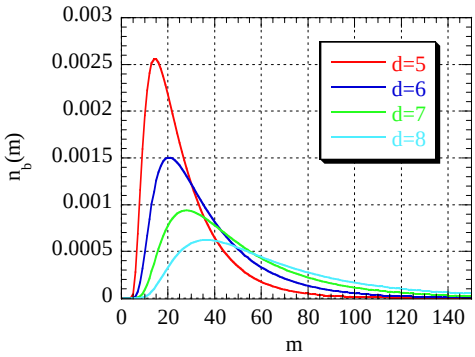

Figure 2.3: The number of bridge-chains with the length m per unit area in the amorphous phase.

population and decreasing monotonically. On the other hand, there is a peak in the distribution of the bridge-chains. Furthermore, for $mb^2 \ll d^2$, $n_\ell(m)$ show power-law decay with the exponent $-3/2$, while for $mb^2 \gg d^2$, both $n_\ell(m)$ and $n_b(m)$ decays exponentially. This implies the existence of the scaling law

$$n(m)b^2 = m^{-3/2}\mathrm{g}\big(mb^2/d^2\big) \tag{2.6}$$

for both $n_\ell(m)$ and $n_b(m)$.

2.2.2 Analytical solution

We further derived analytic solutions for $n_\ell(m)$ and $n_b(m)$ as an infinite series. First, it can be easily shown that the external field $V(x)$ can be written as

$$V(x) = \{\delta(x-\varepsilon) + \delta(x-d+\varepsilon)\}/C^{1/2}. \tag{2.7}$$

This means the chains inside the amorphous phase behaves as just Gauss chains. The end distribution of the chains starting on $x = \varepsilon$ and $x = d - \varepsilon$ can be represented by

$$\mathcal{Q}^{(L)}(s,x) = \frac{2}{d}\sum_{p=1}^{\infty}\sin\left(\frac{p\pi\varepsilon}{d}\right)\sin\left(\frac{p\pi x}{d}\right)\exp\left(-\frac{p^2\pi^2 sb^2}{6d^2}\right) \tag{2.8}$$

$$\mathcal{Q}^{(R)}(s,x) = \frac{2}{d}\sum_{p=1}^{\infty}(-1)^{p-1}\sin\left(\frac{p\pi\varepsilon}{d}\right)\sin\left(\frac{p\pi x}{d}\right)\exp\left(-\frac{p^2\pi^2 sb^2}{6d^2}\right), \tag{2.9}$$

respectively [4]. Determining the normalization constant as it satisfies the condition

$$\sum_{m=1}^{\infty}\sum_{s=1}^{m}\{\phi_\ell^{(L)}(s,x \mid m) + \phi_\ell^{(R)}(s,x \mid m) + \phi_b(s,x \mid m)\} = 1, \tag{2.10}$$

and taking the limit of $\varepsilon \to 0$, the number of loop- and bridge-chains per unit area can be obtained as

$$n_\ell(m) = \frac{\pi^2 b}{9d^3}\sum_{p=1}^{\infty}p^2\exp\left(-\frac{p^2\pi^2 mb^2}{6d^2}\right) \tag{2.11}$$

$$n_b(m) = \frac{\pi^2 b}{9d^3}\sum_{p=1}^{\infty}(-1)^{p-1}p^2\exp\left(-\frac{p^2\pi^2 mb^2}{6d^2}\right). \tag{2.12}$$

The analytic solutions (2.11) and (2.12)are plotted for $d = 5, b = 1$ as well as the numerical results in fig.2.4,fig.2.5, respectively, showing good agreement between these.

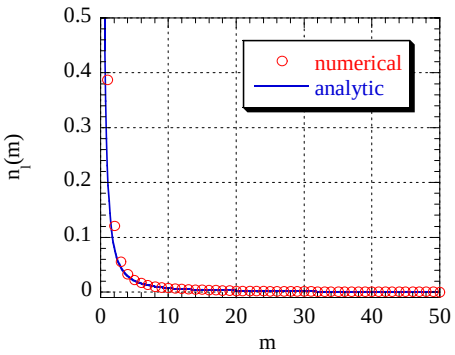

Figure 2.4: Comparison between the numerical result and the analytic solution for the number of loop-chains with the length m within the amorphous phase ($d = 5$) of unit area.

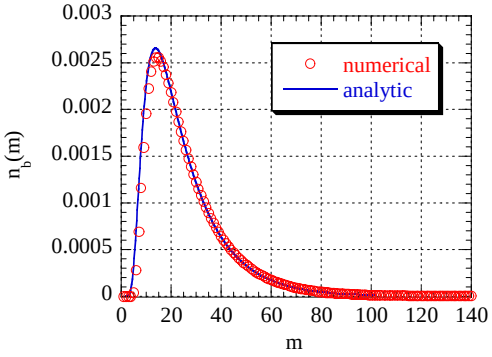

Figure 2.5: Comparison between the numerical result and the analytic solution for the number of bridge-chains with the length m within the amorphous phase ($d = 5$) of unit area.

2.3 Mechanical properties of semi-crystalline polymer

In this section, it is reported that the relationship between the mechanical properties and the morphology of the lamella structures of semi-crystalline polymer by molecular mechanics (MM) and molecular dynamics (MD)simulations. Isotactic polypropylene was chosen for the target. To calculate elastic moduli for both of large and small deformations, firstly we determined potential parameters of the bead-spring model by MM assuming that the density and moduli of lamella structure are determined the potential as well as that of pure crystal. Secondly to handle Three-dimensional realistic structure of the lamella, we developed a novel method to generate the system. Thirdly we investigated elastic moduli of lamella systems using MM for small deformation cases, and compared the results with series/parallel model. Moreover, stress-strain behavior under large deformation were investigated by MD.

2.3.1 Model and Method

Model used in this study is bead-spring model of the type of Grest and Kremer[5], and each bead in the system obeys following equation of motion which Clarke and Brown[6] developed:

$$\dot{\mathbf{R}}_i = \frac{\mathbf{p}_i}{m_i} + \dot{\mathbf{h}}\mathbf{h}^{-1}\mathbf{R}_i \tag{2.13}$$

where $\mathbf{R}$, $\mathbf{p}$, and m are the coordinate, the moment, and the mass of bead, respectively. Transformation matrix $\mathbf{h}$ make up from the basis vectors, $\mathbf{h} = (\mathbf{a}, \mathbf{b}, \mathbf{c})$ which determine the shape of the cell. $\mathbf{h}$ and current pressure $\mathbf{P}$ are controlled by:

$$\dot{\mathbf{h}} = \frac{\mathbf{P} - \mathbf{P}_0}{M} \tag{2.14}$$

$$\mathbf{P} = \frac{1}{V}\sum_{i=1}^{N}(\frac{\mathbf{p}_i\mathbf{p}_i}{m_i} + \mathbf{R}_i\mathbf{f}_i) \tag{2.15}$$

where $\mathbf{P}_0$, M, and $\mathbf{f}$ are target pressure tensor, the constant, and force, respectively. Also Temperature is controlled by loose coupling method[7]. Potential used in this study consists intramolecular part and intermolecular part as follows:

(i)Bond interaction between neighboring beads i and j,

$$\begin{cases} U(r_{ij}) = -\frac{1}{2}k \cdot R_0^2 \cdot ln(1 - (\frac{r_{ij}}{R_0})^2) & r_{ij} \le R_0 \\ \infty & r_{ij} \ge R_0, \end{cases}$$

$$\begin{cases} U(r_{ij}) = 4\epsilon(\frac{\sigma}{r_{ij}})^{12} - (\frac{\sigma}{r_{ij}})^6 + 0.25 & r_{ij} \le 2^{\frac{1}{6}}\sigma \\ 0 & r_{ij} \ge 2^{\frac{1}{6}}\sigma, \end{cases}$$

(ii)Nonbond interaction for all except neighboring beads,

$$\begin{cases} U(r_{ij}) = 4\epsilon(\frac{\sigma}{r_{ij}})^{12} - (\frac{\sigma}{r_{ij}})^6 + U_{shift} & r_{ij} \le \sigma_{cutoff} \\ 0 & r_{ij} \ge \sigma_{cutoff} \end{cases}$$

It is well known that results of MM and MD calculation are significantly affected by the parameters in intramolecular part and intermolecular part (for example, σ, ϵ etc. in Eq.(2.3.1)). To simulate realistic system, we try to determine these parameters by considering experimental results for structure and mechanical properties as follows:

1. Building up of initial structure of pure crystal.
2. Equilibration of the system by MM and MD, with various potential parameters and densities of system which are built by changing the isotropic pressure of the systems.
3. Calculation of elastic moduli under small deformation by MM for each potential parameter.
4. Determination of the potential parameter by comparison of the modulus with experimental data.

With the set of potential parameters obtained by above procedures, elastic moduli for lamella structure are obtained by MM as well as stress-strain behavior under large deformation by MD. For these simulations, a novel generating method of lamella structure on three-dimensional periodic boundary cell is proposed. In the later sections, detail explanation for each step shall be described.

All simulations presented in this study were done by COGNAC. The three-dimensional periodic boundary conditions were applied. MD simulations were carried out in the reduced unit, in which σ, ϵ, and m are taken as the unit of length, energy, and mass, respectively. The unit of time τ, pressure p and density ρ are given by $\tau = \sigma(m/\epsilon)^{0.5}$, $p = \epsilon/\sigma^3$, and $\rho = m/\rho^3$. The temperature k_BT was set at 0.1ϵ, which is sufficiently lower than the melting point. The equation of motions is solved using the velocity Verlet algorithm with the time step $\delta t = 0.001\tau$.

2.3.1.1 Determination of potential parameters

Generation of crystal

In this study, elastic moduli of the material are discussed for pure crystal system to determine the potential parameter used for overall MD calculation of lamella. To generate pure crystal system, initially we put 100 linear chains consisting 10 beads aligned to one specific direction in a periodic boundary cell of $10\sigma \times 10\sigma \times 10\sigma$. Two ends of each chain were connected across the cell by the minimum image distance to achieve infinite molecular weight. (Hence here any effect of defect due to chain ends is not considered.) The system was equilibrated using MD simulation with various potential parameters and pressure. Examined conditions are shown later with calculation results on Table 2.1. After equilibration, energy of the system was minimized by MM simulations.

Calculation of elastic moduli

The pure crystal system generated by the previous procedure was deformed with small strains less than 0.002 to calculate elastic moduli by MM. Elastic moduli are derived from stiffness matrix $\mathbf{C}_{ij}$. For an isotropic material such as an amorphous polymer, $\mathbf{C}_{ij}$ can be expressed by Lamé constants λ, μ as follows,

$$\mathbf{C}_{ij} = \begin{bmatrix} \lambda+2\mu & \lambda & \lambda & 0 & 0 & 0 \\ \lambda & \lambda+2\mu & \lambda & 0 & 0 & 0 \\ \lambda & \lambda & \lambda+2\mu & 0 & 0 & 0 \\ 0 & 0 & 0 & \mu & 0 & 0 \\ 0 & 0 & 0 & 0 & \mu & 0 \\ 0 & 0 & 0 & 0 & 0 & \mu \end{bmatrix}. \tag{2.16}$$

The tensile (Young's) modulus E and the Poisson's ratio ν are given by

$$E = \mu\frac{3\lambda+2\mu}{\lambda+\mu}, \quad \nu = \frac{\lambda}{2(\mu+\lambda)}. \tag{2.17}$$

When the material is planar isotropic, $\mathbf{C}_{ij}$ is given by five constants, k, ℓ, m, n, and μ,

$$\mathbf{C}_{ij} = \begin{bmatrix} n & \ell & \ell & 0 & 0 & 0 \\ \ell & k+m & k-m & 0 & 0 & 0 \\ \ell & k-m & k+m & 0 & 0 & 0 \\ 0 & 0 & 0 & m & 0 & 0 \\ 0 & 0 & 0 & 0 & \mu & 0 \\ 0 & 0 & 0 & 0 & 0 & \mu \end{bmatrix}. \tag{2.18}$$

The tensile modulus E_1 and the Poisson ratio ν_1 in ordered direction are given by

$$E_1 = n - \frac{\ell^2}{k} \tag{2.19}$$

and

$$\nu_1 = \frac{\ell}{2k}. \tag{2.20}$$

On the other hand, the tensile modulus E_2 and the Poisson ratio ν_2 in isotropic directions are given by

$$E_2 = \frac{4m(nk - \ell^2)}{n(k+m) - \ell^2} \tag{2.21}$$

and

$$\nu_2 = \frac{n(k-m) - \ell^2}{n(k+m) - \ell^2}. \tag{2.22}$$

Under the small deformations in which the Hooke's law can be applied, the stiffness coefficients are given by[8],

$$\mathbf{C}_{ij} = \left.\frac{\partial \sigma_i}{\partial \epsilon_j}\right|_{T,\epsilon_j} = \left.\frac{1}{V_0}\frac{\partial^2 A}{\partial \epsilon_i \partial \epsilon_j}\right|_{T,\epsilon_i,\epsilon_j} = \left.\frac{1}{V_0}\frac{\partial^2 U^{pot}_{min}}{\partial \epsilon_i \partial \epsilon_j}\right|_{T,\epsilon_i,\epsilon_j} \tag{2.23}$$

where ϵ is the strain tensor and A is the Helmholtz free energy ($A = U - TS$). In this equation, the entropic contributions are neglected. Consequently the stiffness matrix can be calculated from the second derivatives of potential energy U_{min} of energetically minimized structures using MM simulations.

Based on above discussion, elastic moduli were calculated by MM simulations where the strain was applied by deformation of periodic boundary. Note that here we did not employ affine manner to eliminate the effect of destruction of inner structure of the system, and that the system volume was not conserved because the boundary deformation was performed for each axis of the cell independently. Applied strain was varied within ± 0.002 for each direction.

Comparison with experimental data

To determine the optimum set of the potential parameters, we compare the calculated moduli with experimental values. Direct comparison is, however, not available because the relation between absolute values of the moduli and the parameters is complicated, and to determine it, one should perform tremendous calculation to obtain large number of material constants. To escape from above difficulty, we focused on the ratio of the tensile moduli in the c-axis and in the transverse directions, $\alpha == \frac{E_c}{E_t}$. Value of α was compared with an experiment[9] and suitable potential parameters and density were chosen for MD simulation. The obtained set of the parameters was examined also for an amorphous system consisting one long chain with 1000 beads in periodic boundary by MM.

2.3.1.2 Generating lamella structure

In this section, a novel method to generate lamella structure of semi-crystalline polymer in three-dimensional molecular dynamics simulations. Though various studies have been reported on molecular simulation of lamella, the most of them discussed only the amorphous structure confined in between two crystalline surfaces. For example, Dimarzio, Guttman and Hoffman[2][3] analyzed the population of loop and bridge in amorphous phase between two crystalline phases by random walk model. Gautam, Balijepalli, and Rutledge[10] investigated the topology of the interface between the crystalline phase by off-lattice Monte Carlo simulations. Brown and Clarke[11] built amorphous structures by using random walk between the interfaces of crystalline phase with suspended short chains. In this study, however, our target is realistic situation where crystalline lamella is elongated with coexisting amorphous potion. To achieve such a situation, we developed a method to generate lamella structure with amorphous. The outline of the method is shown below.

1. The long period of the semi-crystalline lamella L and the length of crystalline phase L_c are specified.
2. The densities of crystal phase ρ_c and amorphous phase ρ_a are specified.
3. One end of a chain is placed at arbitrary position in the amorphous phase.
4. From the chain end, position of the sequential beads are determined by random walk within the amorphous phase, without any intermolecular interaction.
5. If position of a bead goes into a crystalline phase, the helical structure of crystal will be generated until the end reaches to the opposite side of the boundary between crystal and amorphous.

6. According to the conformational distribution of loop and bridge obtained in the previous section(2.2) based on the mean field theory, additional beads are generated to create the loop or bridge. Note that the number distribution of the loop also obeys the theoretical one.

7. Step 5-6 are repeated until the number of the beads reaches to the set value. To eliminate defect in crystalline phase, if the chain end is placed in a crystalline phase, the chain is removed and the process is restarted from Step 3 until both of the chain ends are placed in the amorphous phase.

8. Step 3-7 are repeated for the required number of molecules.

9. When the density of either crystalline or amorphous phase differ from setting density by a certain criteria, all molecules in the system is regenerated from Step 3.

10. When above procedures are finished successfully, the excluded volume effect is introduced gradually through the intermolecular potential by MD.

The details of the Step 6 newly developed for COGNAC are explained below. First, the density d_a of the whole amorphous chain which is a sum of the loop and bridge chains obtained from the mean field calculation is given by Eq.2.24.

$$d_a = \frac{\sum_m \{n_l(m) + n_b(m)\} \times m}{L_a} \tag{2.24}$$

Here, $n_l(m)$ and $n_b(m)$ are the existence probabilities of loop and bridge chain of chain length m obtained by the mean field calculation respectively. L_a is the thickness of an amorphous phase. If the existence of free chain, which is not involved in the crystal phase, and the tail chain are ignored, d_a normalized by crystal density will turn into 1.0. The density of crystalline phase/amorphous phase can be set up separately. Therefore, the probability p_a where one chain goes into amorphous phase from crystalline phase, and the probability p_f where one chain does not go into the amorphous phase but returns to crystalline phase (tight folding) are given by eqs.2.25 and 2.26 respectively from the given amorphous density/crystal density ratio r_d.

$$p_a = \frac{r_d}{d_a} \sum_m \{n_l(m) + n_b(m)\} \tag{2.25}$$

$$p_f = 1 - p_a \tag{2.26}$$

The summation term of eq.2.25 corresponds to the number of chains in the amorphous phase par one chain in the crystalline phase if tail chains are ignored, and becomes p_a in the case of $r_d = 1$. However, in this method, there is no distinction of a tight folding and the loop chain of length 1, and supposing that a tight folding always has the amorphous portion of length 1. In this case, density $d'_a (= r_d)$ of all amorphous phases is given by eq.2.27.

$$d'_a = \frac{\left[p_a \sum \{n_l(m) + n_b(m)\} \times m\right] + \left[1 - p_a \sum \{n_l(m) + n_b(m)\}\right]}{L_a} \tag{2.27}$$

Here, the first term in right-hand side comes from the amorphous phase based on the mean field theory and the second term comes from the tight folding. p_a and p_f are derived from eq.2.27 and given by

$$p_a = \frac{r_d L_a - 1}{\sum_m \{n_l(m) + n_b(m)\} \times m - \{n_l(m) + n_b(m)\}} \tag{2.28}$$

$$p_f = 1 - p_a \tag{2.29}$$

Actually, when a chain is extended to the end of a crystalline phase in the process of chain generation, the molecular structure (loop chain/bridge chain, and degree of polymerization m) generated as an amorphous part of the chain is chosen by the Monte Carlo method based on $n_l(m)$ and $n_b(m)$ obtained by the mean field theory. However, in order to take a tight folding into consideration, the p_f obtained by eqs.2.28 and 2.29 is added to $n_l(1)$ obtained by the mean field theory and the summation is used as probability distributions.

The coordinate of an amorphous part of length m in a chain is generated at random, and the trial is repeated until the end segment will reach proper position for loop/bridge conformation.

2.3.1.3 Calculation of elastic moduli for lamella

To obtain overall elastic moduli of the lamella, MM calculation was performed for a system consisting two chains with 500 beads for each. (Hereafter we denote this system as small system.) We set $L = 15\sigma$, $L_c = 10\sigma$, $\sigma_c = 1.11\sigma$, and $\sigma_a = 1.0\sigma$ as initial conditions. Using the scheme presented in the previous section, we generated lamella structures with the determined potential in rectanglar unit cell of $15\sigma \times 7.9\sigma \times 7.9\sigma$.

MD with constant pressure was carried out by changing external pressure up to obtain proper densities for the crystalline phase ρ_c and amorphous phase ρ_a, since it is necessary to eliminate anisotoropic pressure of the system and to relax the overall contortion of the system. If ρ_c and ρ_a remained unchanged for 2000τ, the system is assumed to be equilibrated.

Note that after equilibration of the system the cell deformed spontaneously: it shrinks to c-axis direction and elongates to the perpendicular direction.

To this system MM simulation was applied with small deformation ranging within $\epsilon = \pm 0.002$. We calculated the moduli assuming that the lamella structures were planar isotropic, i. e. the perpendicular directions to c-axis of the crystal are isotropic.

2.3.1.4 Observation of stress-strain behavior of lamella

In order to investigate the stress strain behavior at large deformations by MD, we generated larger system than that for the MM study to obtain elastic moduli in linear regime. The system consists 4 chains with 1200 beads. (Hereafter we denote this system as large system.) We set $L = 20\sigma$, $L_c = 15\sigma$, and $\sigma_c = 1.11\sigma$, and $\sigma_a = 1.0\sigma$ as initial conditions. As well as the MM case, lamella structure was generated by the scheme based on the mean field calculation in unit cell of $20\sigma \times 14.9\sigma \times 14.9\sigma$, and it deformed spontaneously during the equilibration. After the equilibration, it was elongated in c-axis direction (= z direction) of crystalline phase with the strain rate $\dot{\epsilon} = 0.016\tau^{-1}$ up to strain $\epsilon = 1.0$ by MD simulation. During the elongation, pressure in the perpendicular directions to the elongation was controlled, i.e. the lengths of a-axis and b-axis of the unit cell were changed independently to keep the pressure constant, while the angles of the unit cell were fixed.

2.3.2 Results and Discussion

2.3.2.1 Optimal potential parameters

The snapshot of a minimized crystal model used for elastic moduli calculation was shown in Fig.2.6.

Figure 2.6: Snapshot of a minimized crystal of isotactic polypropylene

The averaged tensile modulus of five independent initial conditions was shown in Table2.1.

Table 2.1: Tensile moduli of the crystal model and the amorphous model compared with the experimental results and the result of Theodorou and Suter of polypropylene

crystal	densityρ_c $[m/\sigma^3]$	pressure$P$ $[\epsilon/\sigma^3]$	σ_{cutoff} $[\sigma]$	R_0 $[\sigma]$	k $[\epsilon/\sigma^3]$	E_c $[\epsilon/\sigma^3]$	E_t $[\epsilon/\sigma^3]$	$\alpha = E_c/E_t$
C1	1.00	-3.5	1.5	1.5	30	323.3	10.7	30.2
C2	1.06	-1.3	1.5	1.5	30	1000.1	80.7	12.5
C3	1.11	0.35	1.5	1.5	30	1068.1	103.7	10.3
C4	1.00	-5.5	2.0	1.5	30	935.4	40.1	23.3
C5	1.06	-4.0	2.0	1.5	30	997.3	60.9	16.4
C6	1.11	-2.0	2.0	1.5	30	1052.9	91.7	11.5
exp.						33.3$[GPa]$	2.9$[GPa]$	11.5
amorphous	densityρ_c	pressure$P$	σ_{cutoff}	R_0	k	E_a $[\epsilon/\sigma^3]$		
A1	1.01	-2.0	2.0	1.5	30	25.3		
calc.						94.5 (reduced value)		

One can see that when the density of system ρ_c is 1.11ρ and the cutoff distance σ_{cutoff} is 2.0σ, the suitable ratio of modulus α for experimental one[9] is obtained. The result for an amorphous case is also presented from calculation with the same set of the parameters. Though it is discrepant from the earlier result[8] quantitatively, comparing with the moduli of crystalline, we can say that obtained result for amorphous is reasonable because in this study we focus on the effect of cooperation of coexisting two phases in the lamella on mechanical response, not on the accurate determination of the potential parameters and absolute values of the moduli.

2.3.2.2 Tensile moduli of lamella

A snapshot of the equilibrium structure of the small system is shown in Figure 2.7.

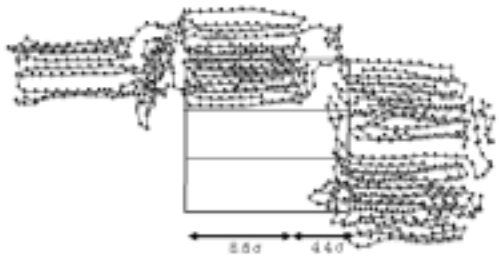

Figure 2.7: Snapshot of the structure of PP semi-crystalline lamella consisting of 2 chains with 500 beads.

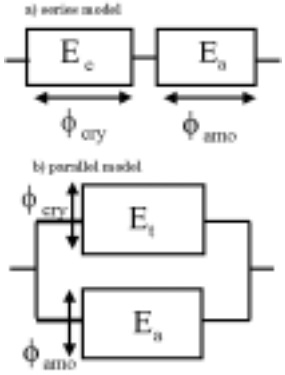

Figure 2.8: Complex mechanical model:(a) series model,(b)parallel model.

The lengths of crystalline phase and amorphous phase obtained after the equilibration were 8.5σ and 4.4σ respectively reflecting the fact that both phases shrank a little in c-axis direction of crystalline phase. It is noteworthy that several distorted and irregular structure in the crystal due to kink conformation, penetration of the amorphous chain, interfacial defects, etc., are observed. The averaged tensile modulus of five independent initial structures obtained by MM is shown in Table 2.2. Also we analyzed two tensile moduli using the series and parallel models (Figure 2.8). Each modulus of the two models is defined as follows:
(a) Series model,

$$E_c^{-1}(lamella) = \phi_{cry}E_c^{-1} + \phi_{amo}E_a^{-1} \tag{2.30}$$

(b) Parallel model,

$$E_t(lamella) = \phi_{cry}E_t + \phi_{amo}E_a \tag{2.31}$$

where E_c, E_t and E_a are the tensile modulus in the c-axis and in the transverse direction of crystal and in amorphous (see Table2.1), and ϕ_{cry} and ϕ_{amo} are volume fractions of crystalline phase and amorphous phase, respectively. These were compared with the averaged tensile modulus of realistic structure in Table 2.2.

It is emphasized that both of $E_c(lamella)$ and $E_t(lamella)$ are well described by the series model. It is peculiar result for the system where crystal and amorphous construct lamella structure. Assuming the situation where the crystal is surrounded by the amorphous, one can easily understand above result so that one possible explanation is interpenetration of the chains in between two phases, as shown in Fig.2.7. It is considered that these distorted structures in the crystalline phase affect the decrease of the tensile modulus in the transverse direction more strongly than in the c-axis direction.

Table 2.2: Comparison of the tensile moduli of the lamella structures of semi-crystalline PP with those estimated from analytical equations of series and parallel model.

	$E_c(lamella)$ $[\epsilon/\sigma^3]$	$E_t(lamella)$ $[\epsilon/\sigma^3]$
realistic lamella structure	71.0	46.3
series model	70.5	48.6
parallel model	701.7	68.9

2.3.2.3 Stress strain behavior

A snapshot of the equilibrium structure of the large system is shown in Figure 2.9(a). The lengths of the crystalline phase and the amorphous phase obtained after the equilibration were 12.8σ and 4.6σ, respectively. Sequential figures during elongation by MD are also presented.

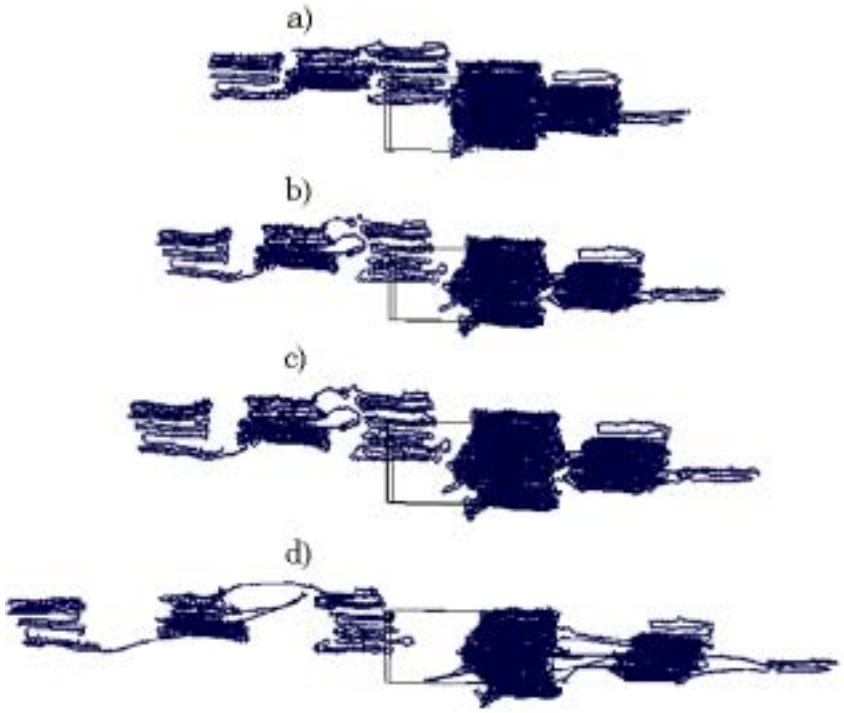

Figure 2.9: Snapshot of the structure of PP semi-crystalline lamella consisting of 4 chains with 1200 beads under elongation in the z direction: (a)strain$\epsilon = 0$ (equilibrium structure),(b)$\epsilon = 0.06$ (at yield point),(c)$\epsilon = 0.30$, and (d)$\epsilon = 1.0$.

The stress in elongational direction (Stress_zz) as a function of strain was shown in Figure refstressstrain-curve. It is observed that the stress steeply increase before a certain strain around 6%, and after the strain the stress gradually decreases to around 1/5 of the peak value. This suggests yield behavior of the system. Corresponding to this observation, the snapshot in Fig.2.9(b) indicates the structural breakage of the crystal. The tensile modulus calculated from the initial slope of the curve and the modulus of the series model were $89.1p$ and $89.9p$ respectively. Consequently we have again verified that the tensile modulus in the c-axis direction of crystalline phase is expressed by a series combination of the moduli of pure crystal

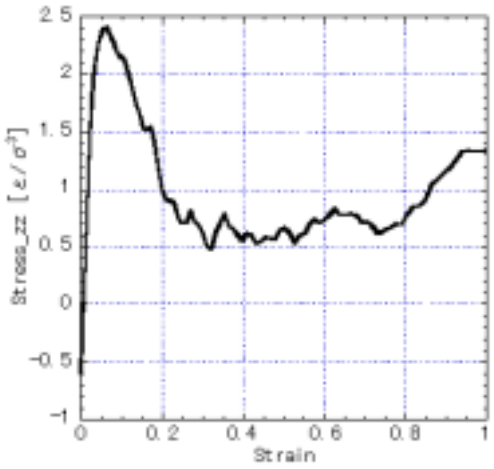

Figure 2.10: Stress-strain curve of PP semi-crystalline lamella model under elongation in the z direction.

and amorphous (see Table2.1).

The stress again increases beyond 30% of strain and it is observed that loose tie molecules in amorphous phase became tight and stretched (see Figure 2.9(d)). The shape of the curve in Figure 2.10 was remarkably close to that of the stress-strain curve of typical semi-crystalline polymer such as isotactic polypropylene[12]. This means that the lamella structure which we generated is close to the realistic structure of semi-crystalline polymer and it is possible to reproduce the mechanical properties of polymer.

2.4 Conclusion

1. The mean field simulation of the distribution of loop/bridge chains of amorphous layer between crystalline layers was performed using the infinite chain model of amorphous layer. Furthermore, the analysis solution which reproduces the probability of the loop/bridge chains of amorphous layer between crystalline layers was obtained.

2. Using the analysis solution from mean field theory, a novel method to generate the lamella structure of semi-crystalline polymer in three-dimensional cell was developed for COGNAC.

3. The potential parameters of the bead-spring model were determined to reproduce the experimental results of the ratio of the tensile moduli in the c-axis and the transverse directions of isotactic polypropylene crystal.

4. Molecular mechanics and dynamics simulations were performed to calculate the mechanical properties. The shape of the stress-strain curve was remarkably close to that of typical semi-crystalline polymer. This means that the lamella structure which we generated is close to the realistic structure of semi-crystalline polymer and it is possible to reproduce the mechanical properties of polymer. The relationship between yielding and the lamella structures of semi-crystalline polymer will be studied in future.

5. Tensile moduli in the c-axis direction and the transverse direction of the crystalline phase are described by the series model. Assuming the situation where the crystal is surrounded by the amorphous, one can easily understand above result so that one possible explanation is interpenetration of the chains in between two phases.

Chapter 3

Bulk elasticity of polypropylene/elastomer blends

3.1 Introduction

Most of general-purpose polyolefin materials are used as polymer blend systems of different species of polymers to get new functions such as the strength, toughness and surface texture. It is known that these polymer blend systems show complicated phase separated structures such as dispersed droplets, fibers and bicontinuous structures depending on the interaction between components, the fraction of blend and the process conditions in blending[13, 14, 15, 16, 17, 18, 19, 20, 21, 22, 23]. It is also found that such phase separated structures strongly influence the mechanical properties, for example, the Young's modulus, tensile strength and impact strength [13, 14, 15, 16]. Therefore, it is important to understand the relation between phase separated structures and mechanical properties. In order to understand this relation, it is indispensable to grasp phase separated structure correctly, but that is sometimes difficult experimentally. For A/B blend systems, the bicontinuous phase exists at a limited region between A droplet/B matrix and the B droplet/A matrix in the phase diagram. However this region is altered by the slight change of physical conditions such as temperature[17, 18, 19, 20, 21]. Furthermore, near the phase transition point, the identification of structure itself becomes difficult. So it is not easy to investigate the relation between phase separated structures and mechanical properties experimentally. On the other hand, in the computer simulation, it is easy to set up various structures and conditions and to change them. For example, it is easily possible to replace both components without changing the structure for a two components system.

Using the our developed simulator "MUFFIN", we investigate the relation between some phase separated structures and mechanical physical properties for polyolefin materials[24]. Moreover, the effect of crystal components which cannot be disregarded in polyolefin materials is also investigated under the phase separated conditions. General-purpose polyolefin materials such as polyethylene and polypropylene are crystalline polymers, which influence the mechanical property due to the significantly large elasticity for the direction of molecular axis [9, 25].

3.2 Model and calculation

We investigate the averaged elastic modulus for various phase separated structures. In order to estimate the averaged elastic modulus, it is necessary to calculate the strain free energy under imposing some displacements. Generally, the free energy F for a linear elastic body can be expressed as a functional of a displacement vector field $u_i(\boldsymbol{x})$ with the following equation

$$\begin{aligned} F\{u_i(\boldsymbol{x})\} &= \int_V f(\boldsymbol{x})dV \\ &\quad - \int_V \rho(\boldsymbol{x})g_i u_i(\boldsymbol{x})dV \\ &\quad - \int_{S_t} T_i(\boldsymbol{x})u_i(\boldsymbol{x})dS, \end{aligned} \tag{3.1}$$

$$f(\boldsymbol{x}) \equiv \frac{1}{2} D_{ijkl}(\boldsymbol{x}) e_{ij} e_{kl}, \tag{3.2}$$

where dV and dS are the body and surface integral respectively and the repeated indices are summed over. $D_{ijkl}(\boldsymbol{x})$, $\rho(\boldsymbol{x})$, g, $T_i(\boldsymbol{x})$, S_t are the local elastic modulus, the mass density, the acceleration of gravity, an external surface load per unit area, the surface being imposed a load respectively. e_{ij} is the strain tensor calculated from the displacement vector and it can be expressed as

$$e_{ij} = \frac{1}{2}\left(\frac{\partial u_j}{\partial x_i} + \frac{\partial u_i}{\partial x_j}\right). \tag{3.3}$$

Polymeric materials are used as polymer blend system of different species of polymers in many industrial applications. In order to treat these systems, it is necessary to treat the mixture of components which have different elastic moduli each other. In our calculation, $D_{ijkl}(\boldsymbol{x})$ is expressed using the elastic modulus tensor D^{α}_{ijkl} and volume fraction $\Psi^{\alpha}(\boldsymbol{x})$ for a component α as

$$D_{ijkl}(\boldsymbol{x}) = \sum_{\alpha} D^{\alpha}_{ijkl} \Psi^{\alpha}(\boldsymbol{x}). \tag{3.4}$$

Using this expression, both an isotropic and anisotropic material can be treated. Of course, the mixture of isotropic and anisotropic materials also can be calculated.

The equilibrium deformation of elastic body can be obtained by minimizing the energy F as

$$\begin{aligned}
\delta F &= \int_V D_{ijkl}(\boldsymbol{x}) e_{kl} \delta e_{ij} dV \\
&\quad - \int_V \rho(\boldsymbol{x}) g_i \delta u_i dV \\
&\quad - \int_{S_t} T_i(\boldsymbol{x}) \delta u_i dS \\
&= \int_V D_{ijkl}(\boldsymbol{x}) \frac{\partial u_k}{\partial x_l} \frac{\partial \delta u_i}{\partial x_j} dV \\
&\quad - \int_V \rho(\boldsymbol{x}) g_i \delta u_i dV \\
&\quad - \int_{S_t} T_i(\boldsymbol{x}) \delta u_i dS \\
&= 0.
\end{aligned} \tag{3.5}$$

The strain free energy density $f(\boldsymbol{x})$ for the isotropic and anisotropic elastic body is described below. Total strain free energy F in the whole system can be calculated by the body integral of $f(\boldsymbol{x})$.

Isotropic elastic body

In the case of the isotropic elastic body such as an amorphous polymer, $f(\boldsymbol{x})$ can be expressed as

$$f(\boldsymbol{x}) = G(\boldsymbol{x})\left(e_{ij} - \frac{1}{d}\delta_{ij} e_{ll}\right)^2 + \frac{K(\boldsymbol{x})}{2}(e_{ll})^2, \tag{3.6}$$

where $G(\boldsymbol{x})$ is the shear modulus and $K(\boldsymbol{x})$ is the bulk modulus. These moduli are calculated using the values G^{α} and K^{α} for a component α and eq.(3.4).

Anisotropic elastic body

In our developed simulator, the systems we can treat are restricted to uniaxial anisotropic elastic bodies. The stress tensor σ_{ij} can be expressed using the strain tensor e_{ij} and elastic moduli, k, l, m, n, μ as

$$\begin{bmatrix} \sigma_{xx} \\ \sigma_{yy} \\ \sigma_{zz} \\ \sigma_{yz} \\ \sigma_{zx} \\ \sigma_{xy} \end{bmatrix} = \begin{bmatrix} n & l & l & 0 & 0 & 0 \\ l & k+m & k-m & 0 & 0 & 0 \\ l & k-m & k+m & 0 & 0 & 0 \\ 0 & 0 & 0 & m & 0 & 0 \\ 0 & 0 & 0 & 0 & \mu & 0 \\ 0 & 0 & 0 & 0 & 0 & \mu \end{bmatrix} \begin{bmatrix} e_{xx} \\ e_{yy} \\ e_{zz} \\ e_{yz} \\ e_{zx} \\ e_{xy} \end{bmatrix}, \tag{3.7}$$

where the x-axis is set as the anisotropic axis. The strain free energy density $f(\boldsymbol{x})$ can be expressed as

$$\begin{aligned} f(\boldsymbol{x}) &= \Big\{ D_1(\boldsymbol{x})\delta_{ij}\delta_{kl} + D_2(\boldsymbol{x})n_i n_j n_k n_l \\ &\quad + \frac{1}{2}D_3(\boldsymbol{x})(\delta_{ij}n_k n_l + \delta_{kl}n_i n_j) \\ &\quad + \frac{1}{2}D_4(\boldsymbol{x})(\delta_{ik}n_j n_l + \delta_{jl}n_i n_k) \\ &\quad + \frac{1}{2}D_5(\boldsymbol{x})(\delta_{ik}\delta_{jl} + \delta_{jk}\delta_{il})\Big\} e_{ij}e_{kl}, \end{aligned} \tag{3.8}$$

where the coefficients D_1, D_2, D_3, D_4, and D_5 have the following relations to n, l, k, m, and μ,

$$\begin{aligned} D_1 &= \frac{k-m}{2} \\ D_2 &= \frac{n+k-m}{2} - l - \mu \\ D_3 &= l - k + m \\ D_4 &= \mu - m \\ D_5 &= m. \end{aligned} \tag{3.9}$$

In order to calculate the equilibrium state for anisotropic elastic materials, it is necessary to give the moduli and the anisotropic axis for each component. Additionally, to get the strain free energy as a result of simulation, it must be given that which direction is assumed to be an anisotropic axis as a whole system.

3.3 Results and discussion

3.3.1 Analysis of simulation results

The displacement vector and the strain energy can be obtained at each mesh point as a result of simulation. Here, the way how to calculate the averaged elastic modulus using the result of simulations is described for an isotropic and anisotropic elastic system.

Treatment as the isotropic elastic system

The system which is regarded as an isotropic structure is considered. In this case, the strain energy F for the whole system can be expressed from eq.(3.6)

$$F = \overline{G}\int \Big\{(e_{ij} - \frac{1}{d}\delta_{ij}e_{ll})^2\Big\}dV + \overline{K}\int \Big(\frac{1}{2}{e_{kk}}^2\Big)dV. \tag{3.10}$$

where, the averaged moduli in the whole system are expressed with an overline. Since a set of three values, F, $\int \big\{(e_{ij} - \frac{1}{d}\delta_{ij}e_{ll})^2\big\}dV$, and $\int \big(\frac{1}{2}{e_{kk}}^2\big)dV$ is obtained as a result of simulation, the averaged moduli $\overline{G}$ and $\overline{K}$ can be estimated using the resultant data for at least two independent deformations. Since eq.(3.10) can be read as the following $y = ax + b$ type equation

$$\overline{K} = -\frac{\int \big\{(e_{ij} - \frac{1}{d}\delta_{ij}e_{ll})^2\big\}dV}{\int \big(\frac{1}{2}{e_{kk}}^2\big)dV}\overline{G} + \frac{F}{\int \big(\frac{1}{2}{e_{kk}}^2\big)dV}, \tag{3.11}$$

$\overline{G}$ and $\overline{K}$ are given by a cross point of lines for various deformation modes.

In the estimation of the averaged moduli, the deformation of "shear", "uniaxial compression", "biaxial compression", and "screw" to the direction of three axes of x, y, and z are carried out. The example of analysis by this method is shown in Figure 3.1.

Treatment as the anisotropic elastic system

Here we focus on an anisotropic system which has an oriented cylinder structure or consists of the oriented crystalline polymer. The way of estimation of the averaged moduli for anisotropic systems is almost the same as that for isotropic systems. In the case of anisotropic system, there are five unknown moduli, n, l,

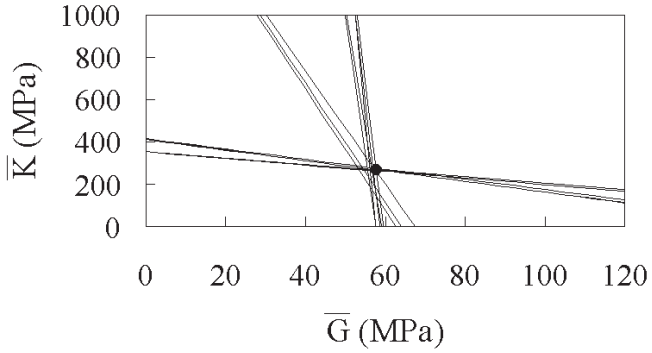

Figure 3.1: Example of the estimation of $\overline{G}$ and $\overline{K}$ (In the case of bicontinuous structure, PP/Elastomer = 30/70). Lines are the results of simulations plotted by eq.(3.11). The cross point of lines is the averaged elastic modulus (symbol shown in figure).

k, m, and μ, and five coefficients, D_1, D_2, D_3, D_4, and D_5. In the similar fashion to the isotropic case, the total strain energy F for the entire system can be expressed using averaged coefficients $\overline{D}_i$ (i=1,...,5) as

$$\begin{aligned} F = \quad & \overline{D}_1 \int \left(\delta_{ij}\delta_{kl}e_{ij}e_{kl}\right)dV \\ & +\overline{D}_2 \int \left(n_i n_j n_k n_l e_{ij}e_{kl}\right)dV \\ & +\overline{D}_3 \int \left(\frac{1}{2}(\delta_{ij}n_k n_l + \delta_{kl}n_i n_j)e_{ij}e_{kl}\right)dV \\ & +\overline{D}_4 \int \left(\frac{1}{2}(\delta_{ik}n_j n_l + \delta_{jl}n_i n_k)e_{ij}e_{kl}\right)dV \\ & +\overline{D}_5 \int \left(\frac{1}{2}(\delta_{ik}\delta_{jl} + \delta_{jk}\delta_{il})e_{ij}e_{kl}\right)dV. \end{aligned} \tag{3.12}$$

Since the total strain energy F and the each coefficient for $\overline{D}_i$ can be obtained as a result of simulation, the coefficient $\overline{D}_i$ can be estimated using the results of simulations for at least five independent deformations. The averaged elastic moduli $\overline{n}$, $\overline{l}$, $\overline{k}$, $\overline{m}$ and $\overline{\mu}$ can be obtained by eq.(3.9). In this evaluation of the elastic moduli, deformations of "shear", "uniaxial compression", "biaxial compression" to the direction of three axes of x, y and z are carried out.

3.3.2 Prediction of the averaged elastic modulus

For the investigation of the influence of phase separated structures on elastic properties for polymer blend systems, the estimation of the averaged elastic modulus was performed by using the multi-component elastic body simulation. Here, the system is assumed to be Polypropylene(PP)/Elastomer polymer blend system to compare the results of calculations with the ones of experiments [21].

3.3.2.1 Simulation conditions

In order to investigate the effect of differences of phase separated structures, two model structures are used. One is the "dispersed structure" where many droplets of the one minor phase disperse in the other major phase, the other is the "bicontinuous structure" where the components are interpenetrated at each other. Additionally, two structures are used for the investigation of the effect of interface. One is the "wide interface (WI) structure" which is gotten from the simulation of our newly developed simulator "SUSHI" based on the Self Consistent Field theory or on the time-dependent Ginzburg-Landau equation. The other one is the "narrow interface (NI) structure" which is obtained by replacing the volume fraction of a component at each mesh point with 0 or 1 by a threshold concentration without changing the structure and total volume

fraction of each component for the WI structure. Each structure is drawn in Figure 3.2a)-c) where the only minor component is shown. The simulations were carried out in the condition PP/Elastomer = 30/70 for all structures. For two model structures, the dispersed and bicontinuous structures, simulations were also carried out in the case where the composition is reversed, namely, PP/Elastomer = 70/30. The elastic moduli of the PP and Elastomer used here are shown in Table 3.1. We used the same elastic modulus for each component as those in the reference [21] to compare the results of calculation with their experiment.

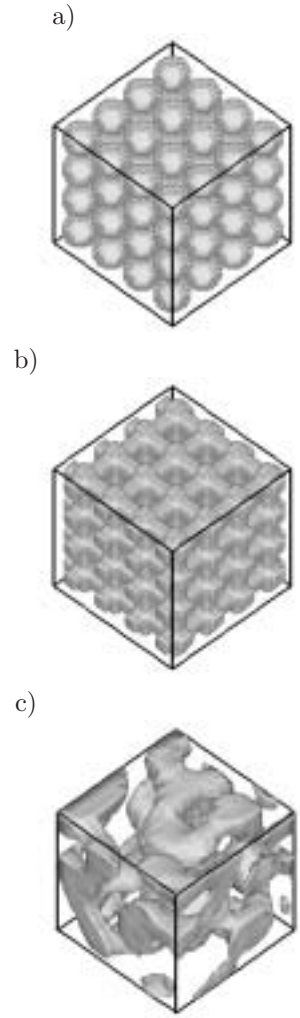

Figure 3.2: Structures used for the prediction of the bulk elastic moduli (The only minor component is shown).

a) Dispersed structure
b) Bicontinuous structure
c) Wide and Narrow interface structure

3.3.2.2 Calculation results

The averaged elastic moduli $\overline{G}$ and $\overline{K}$ for each structure obtained by the simulation are shown in Table 3.2. Using $\overline{G}$ and $\overline{K}$, $\overline{E}$ is calculated using the relation, $E(=(9KG)/(3K+G))$. The value of $\overline{E}$ are also shown in Table 3.2. Moreover, these calculation results are compared with three models, which are parallel, Davies [26], and series models defined by the following equations,

Parallel model:

$$E = \phi_1 E_1 + \phi_2 E_2 \tag{3.13}$$

Table 3.1: Elastic moduli used for the prediction of averaged elastic moduli. ($*E = (9KG)/(3K + G)$)

Component	Symbol	Elastic modulus (MPa)
PP	G	178.57
	K	833.33
	(E	500) *
Elastomer(SEBS)	G	1.0033
	K	100.00
	(E	3.0) *

Table 3.2: Results of prediction of averaged elastic modulus, $\overline{G}$, $\overline{K}$, $\overline{E}$, and corresponding model (PP/Elastomer = 30/70).

Structure	$\overline{G}$ (MPa)	$\overline{K}$ (MPa)	$\overline{E}$ (MPa)	model
Dispersed	1.25	148	3.75	Series
Bicontinuous	11.8	173	34.7	Davies
Wide interface	32.4	185	91.8	
Narrow interface	17.7	137	51.0	

Davies model:

$$E^{1/5} = \phi_1 {E_1}^{1/5} + \phi_2 {E_2}^{1/5} \tag{3.14}$$

Series model:

$$\frac{1}{E} = \frac{\phi_1}{E_1} + \frac{\phi_2}{E_2}. \tag{3.15}$$

The parallel model means that the moduli are given by the simple superposition using the volume fraction of each component as the weight factor. If the additivity rule is realized, this system is considered to be equivalent to a well mixed homogeneous material with the elastic modulus E. Since eq.(3.13) is the same as eq.(3.4), the parts such as the interface where the components are mixed is equivalent to this model in this simulation. On the other hand, the Davies and series models are strongly related to the structure of the system. In many experimental results, Davies model is in agreement with the elastic modulus of bicontinuous structure [27, 15, 28]. The series model is in agreement with the elastic modulus of dispersed structure [21]. The comparison between calculation results and each model is shown in Figure 3.3.

In the case of PP/Elastomer = 30/70, the averaged elastic modulus for bicontinuous structures is higher than that of dispersed structures. The Young's modulus of dispersed and bicontinuous structure are in good agreement with the series and Davies models respectively. These results are also agreement with the experimental results.

The elastic modulus of the WI structure is between the ones of the parallel model and of the Davies model. This is because the WI structure consists of the bicontinuous structure and diffuse interface. On the other hand, in the NI structure where the interface profile is step-like, the modulus decreases and approaches to Davies model. This tendency is due to the reduction of the influence of an interface, and the increase of the influence of the structure. This results means the importance of the width of interface in the polymer blend systems.

In the case of the reversed volume fraction, PP/Elastomer = 70/30, the moduli of dispersed structure increase and the values for both dispersed and bicontinuous structures become very close. The same tendency is also seen in the experimental results [21]. This means that the physical properties for dispersed structure change drastically depending on whether the component with the larger value of E is major or minor.

3.3.3 Calculation of the elasticity of crystalline polymer

It is known that crystalline polymers such as PE and PP have large elastic moduli to the direction of molecular axis. If these polymers are crystallized under suitable conditions, the structure where the anisotropic crystal

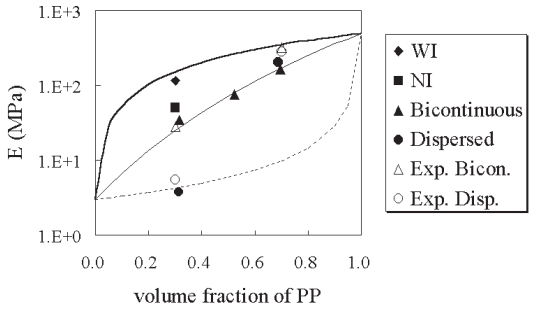

Figure 3.3: Comparison between calculation results of averaged Young's modulus and some models. Opened symbols are the results of this simulation, and Bold, normal, and dashed lines are parallel, Davies, and series model respectively.

Table 3.3: Elastic modulus used for the calculation of elasticity of oriented crystallite.

Component	Symbol	Elastic modulus (MPa)
PP crystal	n	33396.4
	l	438.251
	k	1992.05
	m	1141.73
	μ	377.300
PP amorphous	G	0.50
	K	2000

part separated by an isotropic amorphous part was piled up will be formed. In this case, it has been considered that the mechanical property changes depending on the degrees of orientation of crystallite parts. In order to clarify this dependency, we investigate the mixture of isotropic and anisotropic materials using eqs.(3.1)-(3.5).

3.3.3.1 Calculation conditions

We investigate the averaged elastic modulus for a material with the structure where the cubical crystal domains are surrounded by an amorphous phase as shown in Figure 3.4. Generally, although the crystal part are connected by tie molecules, this effect is neglected here. In order to investigate the influence of orientation of molecular axis, two cases were considered, i.e., (i) the high orientational case, where the anisotropic axis orient to z axis and (ii) the random case. In the high orientaitonal case, the evaluation of the averaged modulus is carried out as an anisotropic system. On the other hand, in the random case, since the system can be regarded as an isotropic material, it is analyzed as an isotropic system. The values shown in Table 3.3 are used in the calculations. These values are obtained by "COGNAC" which is a simulator treating the coarse grained molecular dynamics.

3.3.3.2 Calculation results

In the case of high oriented crystal PP, we obtained the averaged modulus $\overline{E}_1 = 1078$ (MPa) to the direction of molecular axis and $\overline{E}_2 = 57.52$ (MPa) to the direction of perpendicular to molecular axis. On the other hand, in a non-oriented crystal PP, the averaged elastic modulus $\overline{E} = 552.2$ (MPa) is obtained.

In the high orientational case, $\overline{E}_1$ is much smaller than n which is the modulus of the crystal to the direction of the PP chains. This is due to the effect of the PP amorphous component with the small modulus. The same tendency is shown in $\overline{E}_2$. Although the similar decrease of the modulus also occurs in the random case, the value of $\overline{E}$ is between $\overline{E}_1$ and $\overline{E}_2$. This disagreement is considered to be generated from the difference of the degree of orientation of molecules. Although the experimental result which can be

Figure 3.4: Model Structure used for the simulation of crystalline polymer (The only crystal part is shown).

compared with simulation results directly was not found, it is thought that a tendency of simulation result is plausible.

3.4 Conclusion

For polymer blend systems, the relations between phase separated structures and physical properties are very important and complicated. But, it is not easy to understand these relations experimentally. On the other hand, for simulation method, some different phase separated structures with the same volume fraction can be made, and the reverse of component while keeping the phase separated structure can be carried out easily. At this point, it is thought that the numerical approach like in the present study is very important and must be a helpful to understand the relation between structures and mechanical properties.

In the case that the component with low Young's modulus is the minority, the averaged Young's modulus for the bicontinuous structure is larger than that for the dispersed structure with the same volume fraction. On the other hand, the one with high Young's modulus is the minority, the values become almost the same. In the case of the existence of a wide interface, the Young's modulus is larger than the case of the narrower interface. For the crystalline polymer, the elasticity increases as the order of orientation becomes higher.

Chapter 4

Interfacial strength of polypropylene/elastomer blends

4.1 Method and simple application

4.1.1 Introduction

The structure and properties of polymer/polymer and polymer/inorganic interfaces play important roles to mechanical properties such as adhesion and stickiness of polymer thin film. Furthermore, it is well known that the interfacial strength affects bulk properties such as modulus and yield strength of polymer blend and polymer/inorganic composite. In the case of polymer blends, blended polymers overlap each other at the interface and form the interfacial region of certain thickness. The interfacial thickness and the chain conformations of immiscible polymer blends depend on many factors, e.g. miscibility, molecular weight and molecular weight distribution. To study the relation between the interfacial structures and properties of immiscible polymer blend, we conducted coarse-grained molecular dynamics simulation[29].

4.1.2 Model and calculation

In our simulation, we used the bead-spring model of Grest and Kremer [5, 30]. For a blend of A/B homopolymer blend, the interaction potential $U_{ij}(r)$ between two beads of types $i, j = \{A, B\}$ separated by a distance r is given by

$$U_{ij}^{LJ}(r) = \begin{cases} 4\epsilon_{ij}\left[\left\{\left(\frac{\sigma_{ij}}{r}\right)^{12} - \left(\frac{\sigma_{ij}}{r}\right)^{6}\right\} - \left\{\left(\frac{\sigma_{ij}}{r_{cut}}\right)^{12} - \left(\frac{\sigma_{ij}}{r_{cut}}\right)^{6}\right\}\right], & r \le r_{cut} \\ 0, & r > r_{cut}, \end{cases} \tag{4.1}$$

where ϵ_{ij} and σ_{ij} are the Lennard-Jones parameters between bead types i and j, and r_{cut} is a cutoff distance. In the original work of Grest et.al.[30] for binary mixture of polymer blend, r_{cut} is set to $2^{1/6}\sigma$ which takes into account only the repulsive part of the Lennard-Jones potential.

We used two values of r_{cut} between unconnected beads; $r_{cut} = 2^{1/6}\sigma$ and $r_{cut} = 2.5\sigma$, while r_{cut} between connected beads is set to $2^{1/6}\sigma$ in all case.

The diameter of the Lennard-Jones potential, σ_{AA}, σ_{AB} and σ_{BB} are set to 1.0 σ. The energetic parameter ϵ_{AA} and ϵ_{BB} are set to 1.0ϵ and ϵ_{AB} is defined as $\epsilon_{AB} = \epsilon + \delta\epsilon$. Usually, in the case of $r_{cut} = 2^{1/6}\sigma$, $\delta\epsilon$ takes a positive value, since repulsive force between the different type of bead is larger than that between the same type of bead. On the other hand, in the case of $r_{cut} = 2.5\sigma$, $\delta\epsilon$ takes a negative value, since the attractive force between different type of bead is smaller than that between the same type of bead. In both case, when the absolute value of $\delta\epsilon$ becomes larger, the miscibility between beads A and B decreases and the interfacial thickness becomes thiner.

The neighboring beads along the chains are connected by an unharmonic attractive interaction $U^{ch}(r)$:

$$U^{ch}(r) = \begin{cases} -\frac{1}{2}kR_0^2 \ln\left[1 - \left(\frac{r}{R_0}\right)^2\right], & r \le R_0 \\ \infty, & r > R_0 \end{cases} \tag{4.2}$$

where k is the spring constant, and R_0 is the maximum extension of the spring. Following Grest and Kremer, we chose the parameters $k = 30.0\epsilon/\sigma^2$ and $R_0 = 1.5\sigma$. This potential prevents the chains from crossing each other.

For the equation of motion, we used the following Langevin equation [5]

$$m\frac{d^2\boldsymbol{r}_n}{dt^2} = \boldsymbol{F}_n - \Gamma\frac{d\boldsymbol{r}_n}{dt} + \boldsymbol{W}_n(t), \tag{4.3}$$

where m is the mass of the beads, $\boldsymbol{F}_n$ is the force acting on the bead n, Γ is the friction constant, and $\boldsymbol{W}_n(t)$ is a Gaussian white noise which is generated according to

$$\langle \boldsymbol{W}_n(t)\boldsymbol{W}_m(t')\rangle = 2k_BTm\Gamma\delta_{nm}\boldsymbol{I}\delta(t-t'). \tag{4.4}$$

The calculation is carried out in the reduced unit, in which σ, ϵ and m are taken as the unit of length, energy and mass respectively. The unit of time is given by $\tau = \sigma(m/\epsilon)^{1/2}$. The temperature k_BT is set to 1.0ϵ, and the friction constant Γ is set to $0.5\tau^{-1}$ for all cases. Mass of beads is set to $m_A = m_B = 1.0m$. The equation of motion is solved using the velocity Verlet algorithm with time step $\Delta t = 0.012\tau$.

The initial structure of polymer chain at interface is generated by the density biased Monte Carlo (DBMC) method [31, 32] which generates chain configuration for MD simulation from the spatial distribution of each segment of a chain in a phase separate state obtained by the SCF calculation [33, 34]. The chain length N in the MD simulation is taken to be the same as that of the SCF calculation, which means that one segment of the SCF calculation corresponds to one bead of the MD simulation.

In the case of the SCF calculation, one dimensional calculation is conducted and the Neumann (reflective) boundary conditions are applied. To correspond the boundary conditions, staggered reflective boundary conditions [32] for MD simulation are applied to the boundary perpendicular to the interface (z-direction) and periodic boundary conditions are applied to the x,y-direction.

The chain structure and the stress-strain behavior of the interface are studied during elongation. The unit cell length of z-direction is elongated with constant length at certain interval of time step (10-100Δt, which depends on the elongation rate), while the unit cell lengths of x,y-direction are kept constant. The position of beads is moved affinely at the time of deformation of the unit cell. The cutoff distance is set to 2.5σ in the case of studying the behavior during elongation to take into account the effect of attractive force.

All calculations are done by a coarse-grained molecular dynamics program, COGNAC [32] and a dynamic mean field program, SUSHI [35] that we have developed.

4.1.3 Results and discussion

4.1.3.1 Relation between χ and $\delta\epsilon$

We studied the relation between χ and $\delta\epsilon$ using the interfacial thickness as a criterion. The SCF calculation is conducted with certain chain length N and χ and the interfacial thickness and other informations, e.g. a spatial distribution of each segment in a chain are obtained. The initial chain configurations for the MD simulation are generated from the informations of the SCF calculation by the DBMC method. To start the MD simulation, the excluded volume effect has to be introduced since the DBMC does not take into account of the local correlation of the atomic configuration. We introduced the excluded volume effect for the non-bonding interaction and continued the MD simulation with an initial guess of $\delta\epsilon$ which corresponds to the χ. If the interfacial thickness reaches a constant value during the simulation, the equilibrium thickness is thought to be obtained at given $\delta\epsilon$. We continued this procedure and calculated a set of interfacial thickness as a function of χ and $\delta\epsilon$.

In actual calculation, the interfacial thickness L in the case of symmetric polymer blend is given by

$$\phi_i(r) = A\tanh\left(\frac{r\ln 3}{L}\right) + 0.5, \tag{4.5}$$

where r is a position along the axis perpendicular to the interface and set to 0 at the center of the interface, $\phi_i(r)$ is a volume fraction of segment type i at r and A is a coefficient. From this definition, L corresponds to a half distance of total interfacial region. In the case of MD simulation, the volume fraction is calculated by counting the number of beads in a sliced region of unit cell. Then the interfacial thickness L is calculated by the fit with eq.(4.5).

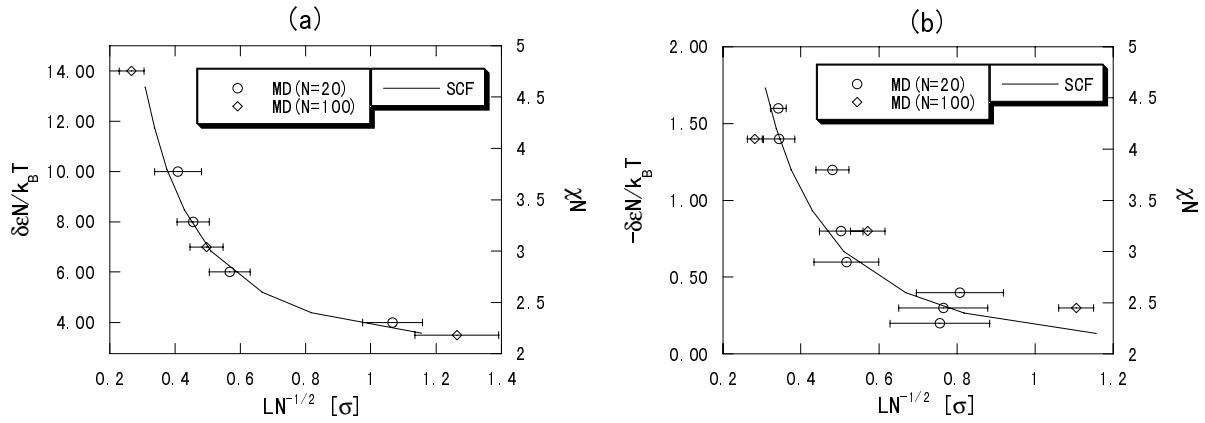

Figure 4.1: Scaled interfacial thickness as a function of $\delta\epsilon N/k_BT$ and χN. (a)$r_{cut} = 2^{1/6}\sigma$ and (b)$r_{cut} = 2.5\sigma$

Two chain lengths, $N = 20$ and 100 are studied. Figure 4.1 shows the scaled interfacial thickness $LN^{-1/2}$ as a function of $\delta\epsilon N/k_BT$ and χN in two cutoff distances. The thickness obtained by the MD simulation is an average of several snapshot structures and the error is shown in the Figure.

A set of pair of $\delta\epsilon N/k_BT$ and χN which gives the same interfacial thickness is selected from Figure 4.1, then the relation between $\delta\epsilon N/k_BT$ and χN is shown in Figure 4.2. The result of Grest et.al.[30] is also shown in Figure 4.2(a).

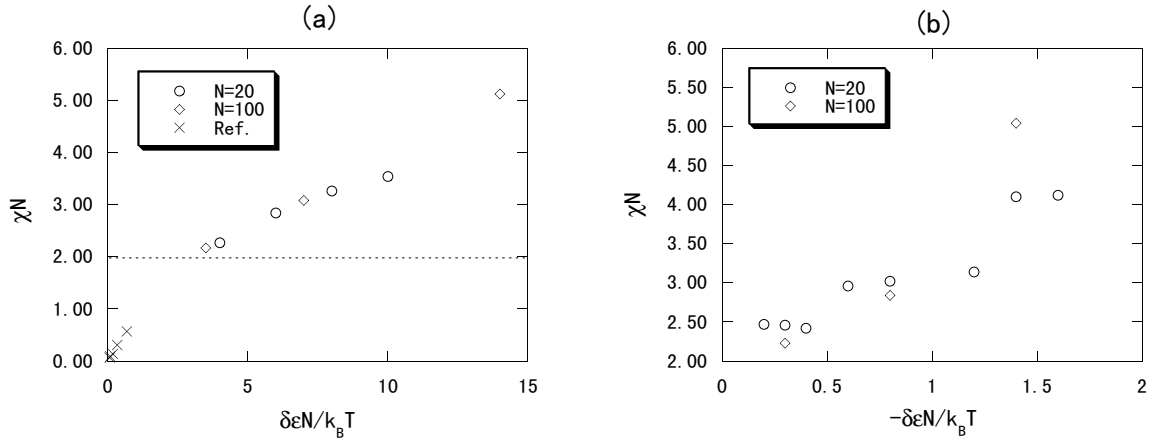

Figure 4.2: Relation between $\delta\epsilon N/k_BT$ and χN. (a)$r_{cut} = 2^{1/6}\sigma$ and (b)$r_{cut} = 2.5\sigma$. The plot 'Ref.' in (a) is the result of Grest et.al.[30]

According to the Flory-Huggins theory [36], χ is given by $\chi = \delta\epsilon z_{eff}/k_BT$, where z_{eff} is an effective coordination number. Grest et.al. reported that the relation between the effective χ and $\delta\epsilon$ in miscible region ($\chi N < 2.0$) is estimated as $\chi_{eff} \approx 1.0\delta\epsilon/k_BT$. In the immiscible region where we studied, the relation between χ and $\delta\epsilon/k_BT$ is clearly different from that of the miscible region. Since the probability of pair distribution of different type of beads will decrease in the phase separated states, the coefficient corresponding to z_{eff} will decrease. Thus, the χ does not increase so much when $\delta\epsilon/k_BT$ increases in the immiscible state comparing to the miscible state as shown in the Figure 4.2(a).

In the case of attractive interaction, the fluctuation of interfacial thickness in the case of the MD simulation is large, and it is difficult to estimate the precise relation between $\delta\epsilon N/k_BT$ and χN. However, $\delta\epsilon N/k_BT$ close to 0 when χN close to a critical point ($\chi N = 2.0$) and the change of $\delta\epsilon N/k_BT$ affects the corresponding χN very much as shown in the Figure 4.2(b). This result suggests that in the case of $r_{cut} = 2.5\sigma$, the small change of $\delta\epsilon N/k_BT$ affects the miscibility very much.

According to the relation between χN and $\delta\epsilon N/k_BT$ obtained in this study, we select several χN and corresponding $\delta\epsilon N/k_BT$ to generate interfacial structures of polymer blend which have a variety of interfacial thickness.

4.1.3.2 Stress-strain behavior

The initial configurations generated by the DBMC method and the following structure relaxation with certain $\delta\epsilon$ of the Lennard-Jones potential are used to study the chain conformation and the stress-strain behavior during elongation of the interface. The numbers of chain $M_{A,B}$ in the case of $N_{A,B} = 20$ and 100 are 40 and 100 respectively. The initial density before elongation is set to 0.85 m/σ^3 in both chain length and the cell sizes are $14.0 \times 14.0 \times 48.0\sigma$ in the case of $N = 100$ and $17.15 \times 17.15 \times 16.0\sigma$ in the case of $N = 20$. The mean square radius of gyration $< R_g^2 >$ of $N = 20$ and 100 are about 5.0 and 25.0 σ^2 respectively and the unit cell sizes are thought to be large enough to reproduce bulk regions at both ends of the unit cell.

$\delta\epsilon N/k_BT$ is chosen as $0.0, -0.3, -1.4$ and -10.0. The case of $\delta\epsilon N/k_BT = 0.0$ corresponds to the homopolymer bulk, since the interaction between a pair A-B is the same as that of A-A and B-B. From the relation obtained by our study, the cases of $\delta\epsilon N/k_BT = -0.3$ and -1.4 correspond to $\chi N = 2.46$ and 4.1 respectively. The case of $\delta\epsilon N/k_BT = -10.0$ corresponds a very strong segregation and the interfacial thickness is very thin.

The initial strain rate $\dot{e}$ is changed from $2.08 \times 10^{-3}\tau^{-1}$ to $2.08 \times 10^{-5}\tau^{-1}$. The relative value of the strain rate comparing to the relaxation time of polymer chain is important to determine the state of polymer, i.e. melt or glassy state, during elongation. The Rouse relaxation time τ_R of $N = 20$ chain is calculated as $460\tau(\tau_R^{-1} = 2.2 \times 10^{-3}\tau^{-1})$ from the Normal coodinates analysis of homopolymer melt. In the case of $N = 100$ chain, the relaxation does not show a simple Rouse relaxation because of the entanglement. Thus, by fitting the autocorrelation function of the Normal coodinates with the KWW equation, the relaxation time τ_r of $N = 100$ chain is estimated to $3.3 \times 10^4\tau(\tau_r^{-1} = 3.0 \times 10^{-5}\tau^{-1})$. Although the strain rate will change during elongation, since the unit cell is elongated at the constant deformation rate ($dz/dt = const.[\sigma/\tau]$), the order of magnitude of the strain rate can be compared to the relaxation time. The fastest elongation rate studied here is comparable to the Rouse relaxation time of $N = 20$ chain and the slowest one is comparable to the relaxation time of $N = 100$ chain.

Figure 4.3 shows the stress-strain behavior of $N = 100$ chain as a function of $\delta\epsilon N/k_BT$. The results of two different $\dot{e}$ are shown in the Figure.

Figure 4.4 shows corresponding snapshot structures of interface of polymer blend before and after elongation. The structures in the case of the initial elongation rate $\dot{e} = 2.08 \times 10^{-4}\tau^{-1}$ are shown in the Figure.

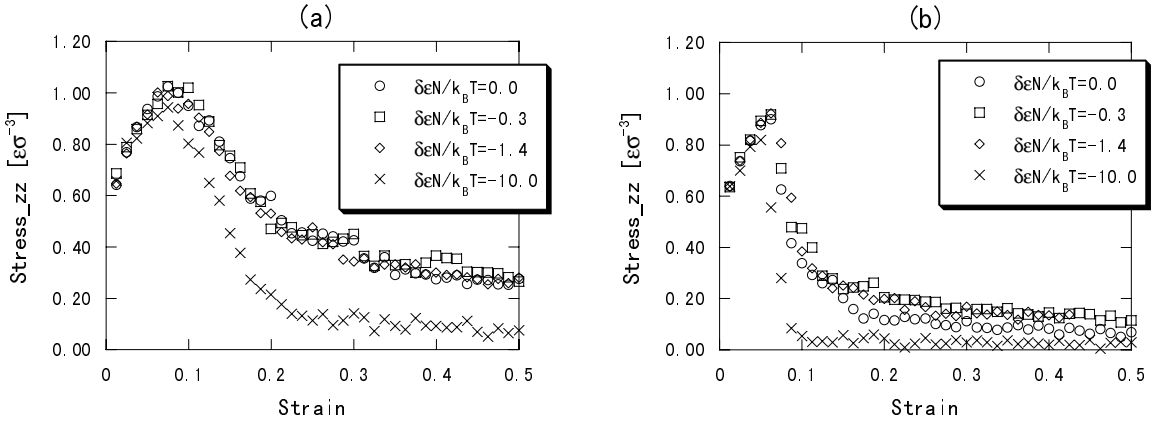

Figure 4.3: Stress-strain curve of polymer blend at interface as a function of $\delta\epsilon N/k_BT$. Initial strain rate, (a) $\dot{e} = 2.08 \times 10^{-3}\tau^{-1}$ (b) $\dot{e} = 2.08 \times 10^{-4}\tau^{-1}$

In both cases, the stress-strain behavior looks almost the same as that of homogeneous bulk($\delta\epsilon N/k_BT = 0.0$) except for the case of $\delta\epsilon N/k_BT = -10.0$. In the case of $\delta\epsilon N/k_BT = -10.0$, the interfacial thickness is very thin as it is shown in Figure 4.4(b), and the strength of the interface becomes weak. In the case of $\delta\epsilon N/k_BT = -1.4$, the thicknesses of interface L are 1.54 ($N = 20$) and 3.45 ($N = 100$) and the length of the interface region is comparable to R_g.

When the attractive interaction between two polymers are strong and the interfacial thickness is thick enough, bulk failure is observed during elongation as it is shown in Figure 4.4(a). Furthermore, a fibril like structure is observed during elongation. On the other hand, in the case of strong segregation, the fracture

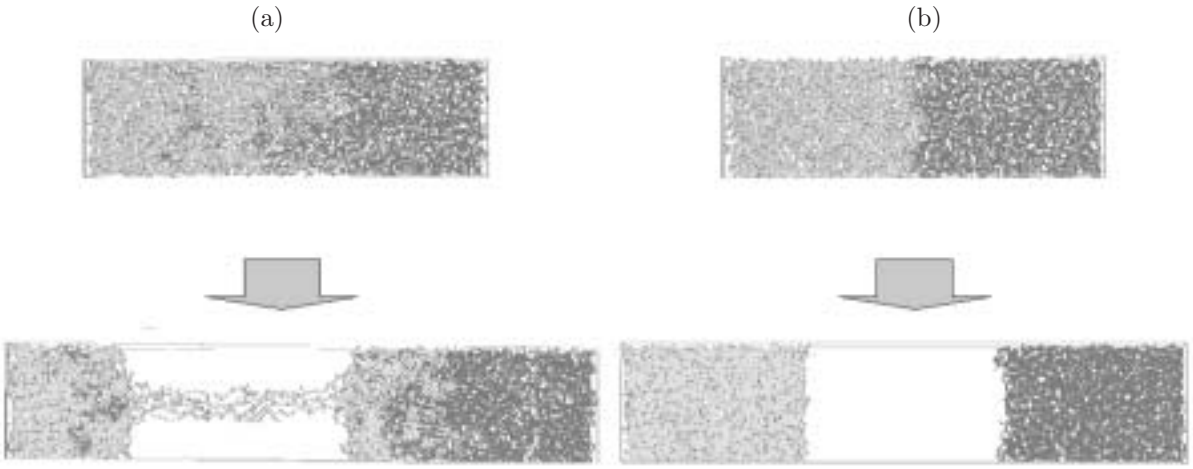

Figure 4.4: Snapshot structures of interfacial structure of polymer blend before(upper) and after(lower) elongation, (a) thick interface ($-\delta\epsilon N/k_BT = 0.3$), (b) thin interface ($-\delta\epsilon N/k_BT = 10.0$).

of interface is observed as it is shown in Figure 4.4(b).

These differences of the chain conformation during elongation explain the stress-strain behavior of different interfacial thickness. When the interfacial thickness is thick enough, the blended polymer chains overlap each other at the interface as well as bulk regions. Thus, the stress-strain behavior is considered to be almost the same as that of homogeneous bulk and the bulk failure takes place even in the case of the polymer blend. We should notice that the difference of attractive energy between A-B and A-A(=B-B) is very small, i.e. $\delta\epsilon/k_BT = -0.014$ in the case of $\delta\epsilon N/k_BT = -1.4$ and $N = 100$, while ϵ_{AA}/k_BT and ϵ_{BB}/k_BT are 1.0. Thus the effect of the difference of attractive energy to the stress behavior can be negligible.

Figure 4.5 shows the stress-strain behavior as a function of chain length N. $\delta\epsilon N/k_BT$ is set to -1.4 and the results of two different $\dot{e}$ are shown in the Figure.

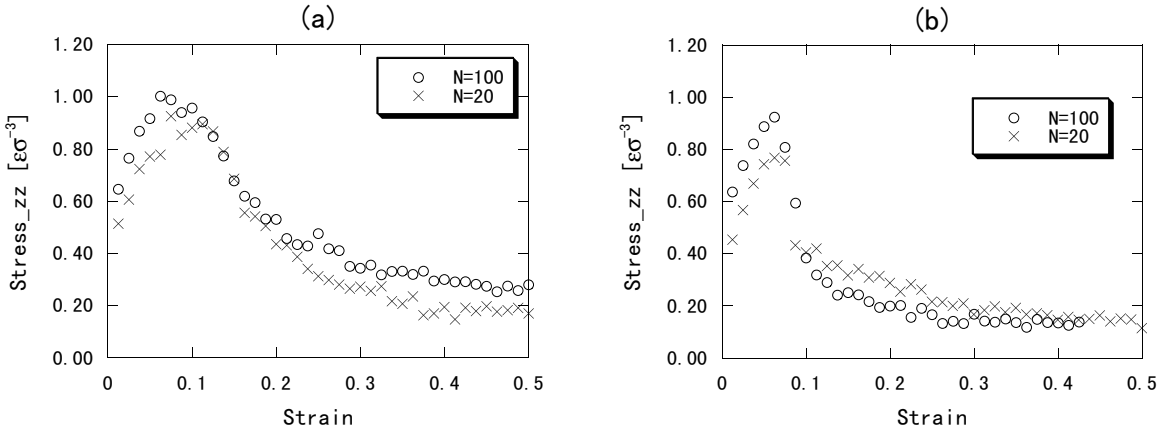

Figure 4.5: Stress-strain curve of polymer blend at interface as a function of chain length N. Initial strain rate, (a)$\dot{e} = 2.08 \times 10^{-3}\tau^{-1}$ (b)$\dot{e} = 2.08 \times 10^{-4}\tau^{-1}$

In both cases, the maximum yield stresses are larger in the case of $N = 100$. However the behavior in the tail region is different, i.e. in the case of fast elongation ($\dot{e} = 2.08 \times 10^{-3}\tau^{-1}$) (Fig.4.5(a)), stress of $N = 100$ is higher than that of $N = 20$, while in the case of slow elongation ($\dot{e} = 2.08 \times 10^{-4}\tau^{-1}$) (Fig.4.5(b)), stress of $N = 20$ is higher than that of $N = 100$. These results are explained as follows. In the case of fast elongation, strain rate is faster than the relaxation time of polymer chain in both chain length, and both polymer chain behave as a glassy state. Thus the longer chains show higher stress at all region because of the higher overlap of chains and strong attractive force between chains. On the other hand, in the case of

slow elongation, since the Rouse relaxation time of $N = 20$ chains is faster than the elongation rate, $N = 20$ chains behave as a melt state. Thus the viscous effect keeps stress higher at the tail region.

Figure 4.6 shows snapshot structures of interface of polymer blend before and after elongation. The structures in the case of $\dot{e} = 2.08 \times 10^{-4}\tau^{-1}$ are shown in the Figure.

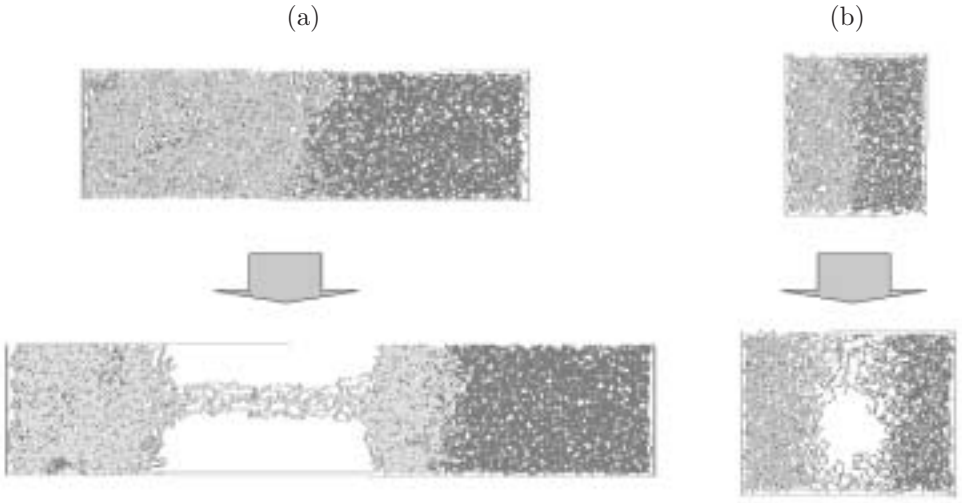

Figure 4.6: Snapshot structures of interfacial structure of polymer blend before(upper) and after(lower) elongation, (a) N=100 (b) N=20

It is observed in the Figure 4.6 that $N = 20$ chains behave as a melt state and flow without chain orientation, while $N = 100$ chain will orient and shows fibril like structure during elongation.

Figure 4.7 shows stress-strain behavior as a function of strain rate. $\delta\epsilon N/k_BT$ is set to -1.4 and the results of different N are shown in the Figure.

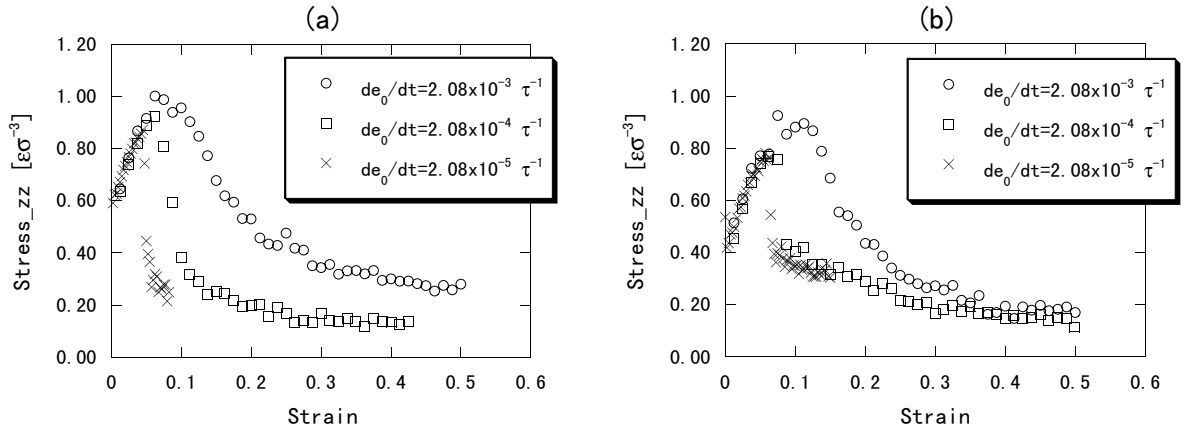

Figure 4.7: Stress-strain curve of polymer blend at interface as a function of initial strain rate. (a)N=100 and (b)N=20

In the case of $N = 100$ (Fig. 4.7(a)), the maximum yield stress and the strain at the yield point increase as strain rate increases, since the relaxation time of polymer is longer than the strain rates in all cases. On the other hand, in the case of $N = 20$ (Fig. 4.7(b)), different results are obtained, i.e. in the cases of $\dot{e} = 2.08 \times 10^{-4}\tau^{-1}$ and $2.08 \times 10^{-5}\tau^{-1}$, the stress-strain behaviors are the same and only in the case of the fastest strain rate, the yield stress and the strain at the yield point increase. Since the Rouse relaxation time of $N = 20$ chain is faster than $2.08 \times 10^{-4}\tau^{-1}$, the system behaves like pure melt state and there is no effect of strain rate, in the case of two slower strain rate.

4.1.4 Conclusion

We studied the interfacial structure and properties of polymer blend with coarse-grained molecular dynamics simulation. The initial structures of the interface are generated efficiently from the informations obtained by the SCF calculation. Furthermore, from the relation between χ parameter and the Lennard-Jones parameter, we generated equilibrium interfacial structures which give consistent interfacial thickness with the results of the SCF calculation.

Using generated interfacial structure of polymer blend, we conducted non-equilibrium MD simulation and studied the chain conformation and stress-strain behavior during elongation of interface. In the case of strong segregation and thin interface, we observed fracture of interface and the low yield stress. On the other hand, in the case of weak segregation and thick interface (thickness being comparable with R_g), the yield stress becomes almost the same as that in the case of homopolymer bulk and the bulk failure is observed. The effects of chain length and strain rate to the stress-strain behavior are also studied. The maximum yield stress increases as the chain length increases and the yield stress and the strain at the yield point increase as the strain rate increases when the strain rate is faster than the longest relaxation time of the polymer.

This simulation method can be applied to study the interfacial properties of more realistic materials. For examples, the effect of molecular weight distribution and additive such as a copolymer to the interfacial properties can be studied.

4.2 Application to a practical system

4.2.1 Introduction

The process of polymer blending is now widely applied for creating new industrial materials. The actual designing of such polymer blends is, however, still a challenging problem. Most polymer blends are immiscible and form macroscopically phase-separated domain structures since the entropy of mixing is negligibly small due to the very large molecular weights of the constituent polymers. In order to realize the good mechanical performance of the blends, it is desirable to have a fine dispersion of the domains and to have strong adhesion between the matrix and the dispersed domains at the interfaces to avoid breaking at a low stress level[37, 38, 39]. One of the approaches to improve the mechanical properties of the immiscible polymer blends is to add suitable block copolymers as compatibilizers. Although adding such copolymers is effective in enhancing the miscibility and in improving the toughness of the interfaces, synthesizing desired block copolymers is rather expensive. Consequently, their use in the large-scale industrial application is quite limited. In a recent experimental study[40] on a polyolefin blend system, a new technique to improve the interfacial strength without using the block copolymer is proposed. In this technique, the molecular weight distribution is controlled so that the distribution of the polymers at the interface is appropriately adjusted. Thus, if the effects of the chain architecture on the interfacial properties are clarified, this technique would have a significant effect on the fabrication technology of the polymer blends. In recent years, a simulation method named as the density-biased Monte Carlo (DBMC) method[31] has been developed to analyze the interfacial peel behavior of immiscible homopolymer blends. The DBMC method is a combination of the coarse-grained molecular dynamics (MD) calculation and the self-consistent mean field (SCF) calculation[33, 34]. In the mean field theory, a many body problem in a dense polymer system is reduced to a problem of independent polymers in an average potential, which represents the influence of the other chains. The advantage of the SCF method is that it can give the density profiles of the constituent polymers that correspond to the equilibrium ground state of the free energy. Using such equilibrium density profiles of the polymers near the interface, we can calculate the overall width of the interfacial region. The DBMC method allows us to generate an equilibrium microscopic chain conformation near the interface, which can be used as the initial state for a MD simulation on the chain deformation behavior under an external field. In this study, the method is applied to immiscible polymer blends with polydispersity[41]. The effects of polydispersity on the interfacial peel behavior are investigated using the SCF simulation code named SUSHI[35]. On the other hand, the microscopic dynamic simulations are done using the coarse-grained MD simulation program named COGNAC[32].

4.2.2 Model and calculation

4.2.2.1 Calculation model

Symmetric A/B binary homopolymer mixtures where both polymers have the same bimodal molecular weight distributions are considered in this study. We assume that each polymer species is composed of two types of chains each of which has different chain length, i.e. N_1 and N_2 ($N_1 < N_2$). Thus, the system is essentially a quaternary mixture. To study the effects of polydispersity, we focus on the difference in the chain length between the longer chains and the shorter chains, and keep the volume fractions of each type of chain fixed as 0.25, respectively. Then, the control parameters of the system are the segment interaction parameter χ_{AB}, the length of the short chain N_1 and that of the long chain N_2, where the segment size b is fixed as 1 for all the segment types. The equilibrium interfacial structure of such a polymer blend is obtained by the 1-dimensional static SCF calculation with the Neumann boundary conditions. This method allows us to calculate the spatial distributions of the segments near the interface.

4.2.2.2 Preparation of the initial structure for the MD simulation

Using the density distribution of each segment obtained by the SCF calculation, the initial conformations of the polymer chains near an interface is generated by the DBMC method[31, 32]. For the MD calculation, we use the bead-spring model of Grest and Kremer [5, 30]. The chain length in the MD simulation is taken to be the same as that of the SCF calculation, which means that one segment of the SCF calculation corresponds to one bead of the MD simulation. To realize the boundary conditions of the MD simulation that corresponds to those used in the SCF calculation, staggered reflective boundary conditions[32] is used for the boundaries parallel to the interface (at the both ends of the z-axis, where z-axis is perpendicular to the interface) and

the periodic boundary conditions for the x and y-directions, respectively. The Lennard-Jones parameter is determined so that the MD simulation can give a consistent result on the interfacial thickness to that obtained in the SCF calculation.

4.2.2.3 Calculation of stress-strain behavior at the interface

The microscopic interface structure created with the above technique is then subjected to an external deformation stress. The relaxation process under the external deformation is simulated using the MD simulation technique, where the simulation box and the chains are deformed affinely in the perpendicular direction to the interface (z-direction) at every fixed time steps while keeping the size of the simulation box in the parallel direction to the interface constant. The change in the chain conformation and the stress-strain behavior of the interfacial region under such an elongation is studied.

4.2.3 Results and discussion

4.2.3.1 Effect of polydispersity on the equilibrium structure of the interface

The equilibrium structure of the interface in such a polymer blend was obtained using the SCF method. Detailed analysis of the free energy and the segment distribution demonstrated that the interface becomes broader when the Flory-Huggins interaction parameter becomes smaller. We also confirmed that the influence of the polydispersity on the density profile of each type of polymers is negligibly small as long as the number-averaged molecular weight M_n is kept constant. Figure.4.8 shows the calculated density profile of the K-type chains $\phi_K(z)$ for both a monodisperse system and a polydisperse system.

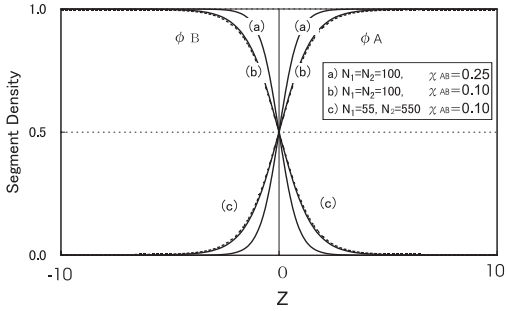

Figure 4.8: Equilibrium density profile near the interface obtained from the SCF calculation for a monodisperse system (solid line) and a polydisperse system (dotted line). These systems have the same number-averaged molecular weight 100.

As the interfacial thickness calculated using the data on $\phi_K(z)$ of a monodisperse system plays a very important role in the DBMC method, we investigate the influence of the polydispersity on the interfacial thickness when the parameter χ_{AB} is changed. The interfacial thickness D of the polydisperse system is determined by fitting $\phi_K(z)$ obtained from the SCF calculation to the following equation.

$$\phi_K(z) = A \tanh\left(\frac{2z}{D}\right) + 0.5, \tag{4.6}$$

where z is the coordinate perpendicular to the interface whose origin is set at the center of the interface, and A is a constant coefficient. Based on the Flory-Huggins model combined with the random phase approximation (RPA), Broseta and coworkers[42] derived the following expression of the interfacial thickness of a monodisperse A-B binary polymer mixture as a function of the molecular weight.

$$D = D_\infty \left(1 - \frac{2\ln 2}{\chi_{AB}}\left(\frac{1}{N_A} + \frac{1}{N_B}\right)\right)^{-\frac{1}{2}} \tag{4.7}$$

$$D_\infty = \frac{2b}{\sqrt{6\chi_{AB}}}, \tag{4.8}$$

where D_∞ is the interfacial thickness in the limit of infinite molecular weight, b is a statistical segment length, and both N_A and N_B are the lengths of the A-polymer and the B-polymer. The numerically evaluated values

of D using the SCF calculation are compared with those predicted by eqs. (4.7) and (4.8). The results are shown in fig.4.9. For the theoretical analysis of our polydisperse system, we assumed N_A and N_B to be both 100. As is shown in fig.4.9, the SCF simulation showed very little effects of the polydispersity on the interfacial thickness. Instead, the interfacial thickness is determined only by the number-averaged molecular weight. Then, the Lennard Jones interaction parameter was adjusted for the polydisperse system so that the DBMC simulation can reproduce the interfacial thickness D obtained by the SCF calculation.

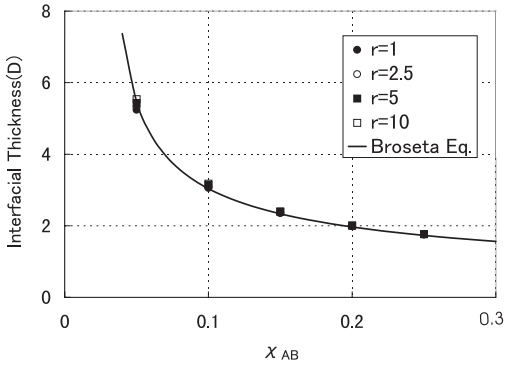

Figure 4.9: Influence of the ratio of the chain lengths between the long chain and the short chain (r) and that of χ_{AB} on the interfacial thickness D of the polydisperse system. The theoretical results obtained with the use of eqs.(4.7) and (4.8) are also shown. In all the simulations, the number-averaged molecular weight is kept constant at 100.

Figure 4.10 shows the effect of the polydispersity on the segment density profile of the A polymer obtained from the DBMC calculation and the SCF calculation, respectively. In these simulations, we set the values of the Lennard Jones interaction parameters as 0.95 and 0.90 that correspond to $\chi_{AB} = 0.10$ and 0.25, respectively. We can confirm that the segment density profiles of each polymer for the polydisperse system are well reproduced by the DBMC simulations. On the other hand, the SCF calculation demonstrates that,

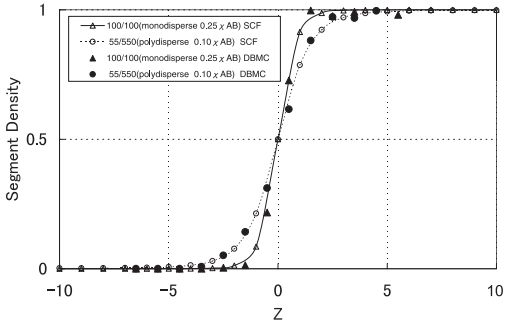

Figure 4.10: Equilibrium density profile near the interface obtained with the DBMC method and with the SCF method.

in the polydisperse system, the depletion of long chains at the interface takes place and the short chains preferentially locate at the interface. Both the segment density of the long chains and that of the short chains were also obtained using the SCF calculation. Figure 4.11 shows the excess density profile of the short and the long chains with different chain length ratio under the same χ_{AB} and M_n. The excess density profile of both short and long chains $\phi_i^{excess}(z)$ are determined as follows.

$$\phi_i^{excess}(z) = \phi_{Ai}(z) + \phi_{Bi}(z) - \phi_{Ai}^{\alpha} - \phi_{Bi}^{\alpha}, \tag{4.9}$$

where the short and long chains are specified by the index i $(i = 1, 2)$, and the segment density of the Ki type chains in the α-type bulk phase is denoted as ϕ_{Ki}^{α}, α specifying one of the coexisting equilibrium phases.

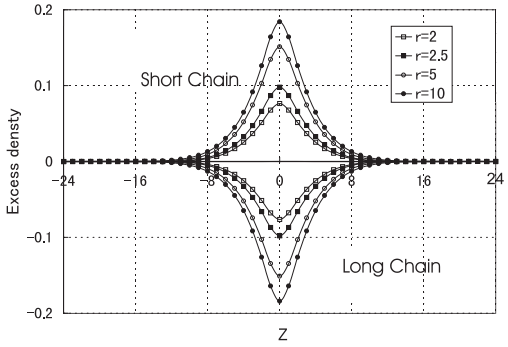

Figure 4.11: Excess density profile of a polydisperse system for various values of the chain length ratio (r). The parameters χ_{AB} and M_n are set as 0.10 and 100, respectively.

The origin of these results can be understood from the entropic point of view. The loss of conformational entropy due to the confinement of the chain at the interface is larger for the long chains than the short chains. As a result, the long chains are tend to be expelled from the interfacial region, and a depletion zone of the long chains is formed at the interface. Such a depletion zone becomes more significant for larger value of r. Typical density profiles of the segments belonging to each type of chains obtained from the DBMC simulations and from the SCF simulations are shown in fig.4.12. We can confirm that the DBMC results agree well with the SCF results, and also that the DBMC can generate the equilibrium conformation of each chain successfully.

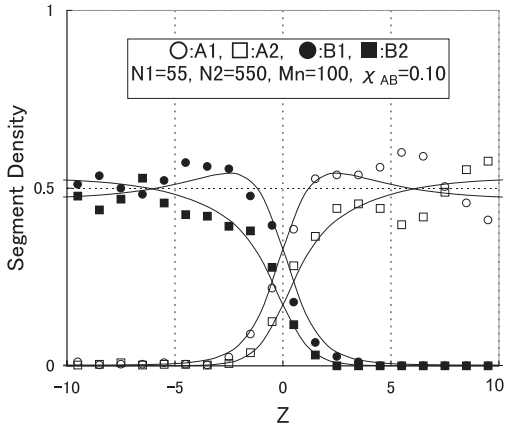

Figure 4.12: Typical density profiles of the segments belonging to each type of chains obtained from the DBMC simulations (symbols) and from the SCF simulations (curves).

4.2.3.2 Effect of polydispersity on the stress-strain behavior of the interfaces

On the basis of the SCF calculation, we found that in the polydisperse system, the depletion of long chains at the interface takes place and the short chains preferentially locate at the interface. These findings mean that the interfacial structure of a polydisperse system is different from that of monodisperse one even if the interfacial thickness is almost the same. Then we analyzed the interfacial peel behavior using model polymer blend systems with different interfacial thickness and the polydispersity. Three model systems were considered. The model-1 and model-2 are monodisperse systems with the same number-averaged molecular weight M_n but have different values of the interaction parameter. The model-3 is a polydisperse system with the same values of M_n and χ_{AB}. In each model, the number-averaged molecular weight was kept constant and the interfacial thickness was controlled by the χ_{AB} parameter. The stress-strain curves and the snapshot pictures of the interfacial region after the elongation are shown in fig.4.13. A yielding point is clearly observed in each case. We found that the yield stress and the yield strain of the monodisperse

system increase with increasing interfacial thickness. On the other hand, for the system with large interfacial thickness, both the yield stress and the yield strain become smaller than those for the monodisperse system with the same interfacial thickness. From the observation of the structure after the elongation, we found that the yield phenomenon of the polydisperse system is dominated by the failure of the interface where the long chains are depleted. On the other hand, for the monodisperse system, the yield phenomenon is dominated by a void formation in the bulk phase.

A possible reason for the influence of the polydispesity on the peel behavior is as follows. The interfacial thickness is a measure of the overlap between the chains belonging to each phase separated by the interface. In comparison to the monodisperse blend case, when the thickness is large enough, a remarkable improvement of the interfacial strength is observed. Because the number of segments between adjacent entanglement points along the chain is about 35 in the present MD simulations[5], the shorter chains are expected to contribute to the interfacial strength only slightly, and the fracture behavior is dominated by the overlap of the long chains. According to the above SCF approach, the overlap of the long chains in the interfacial region will be reduced by the effect of the depletion and will increase with decreasing chain length ratio.

Therefore significant reinforcement of interfacial strength is expected when the molecular weight distribution is narrow enough to have a considerable overlap between the long chains from the both sides of the interface.

These simulation results do not contradict with the recent experimental study reported by Chaffin et.al[40, 43]. They have demonstrated that the narrower molecular weight distribution is effective in improving the peeling behavior of polyolefin blend systems. To obtain a qualitative understanding on the fracture mechanism of polymer interfaces on the molecular scale, further analysis of the entanglement point density at the interface[11] is under way.

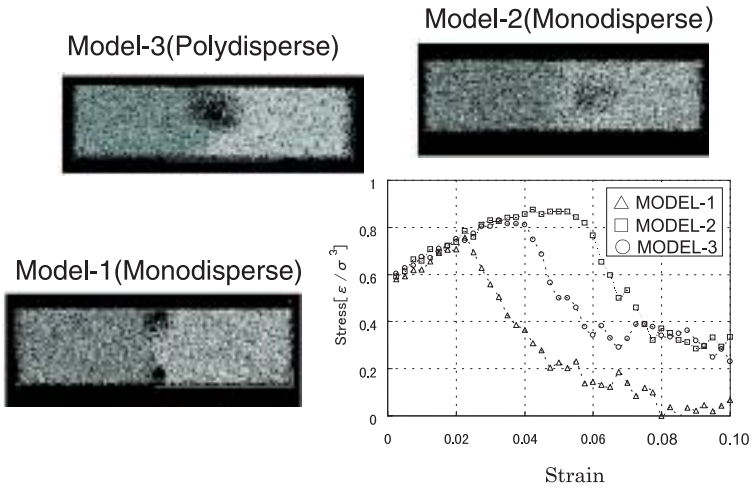

Figure 4.13: Stress-strain curves and the snapshots of the interfacial structure after the elongation. Model-1: $N_s = N_l = 100$, $\chi_{AB} = 0.25$, Model-2: $N_s = N_l = 100$, $\chi_{AB} = 0.10$, Model-3: $N_s = 55$, $N_l = 550$, $\chi_{AB} = 0.10$

4.2.4 Conclusion

In this study, we performed a series of simulations on the interfacial mechanical behavior of an immiscible polymer blends with polydispersity based on a combined technique of the coarse-grained molecular dynamics (MD) simulation and the self-consistent field (SCF) calculation. We confirmed that the simulations can reproduce the experimental data. The equilibrium microscopic chain conformation at interface can be efficiently generated from the spatial distribution of each segment obtained by the SCF calculation, when the Lennard-Jones interaction parameter is adjusted so that the DBMC simulation can reproduce the interfacial thickness obtained by the SCF calculation. The stress-strain behavior under a simple extensional deformation of the interfacial region is simulated using the MD technique. In polydisperse system, it is observed that the depletion of the long chains takes place at the interface where the short chains preferentially locate. Significant reinforcement of the interfacial strength is observed when the molecular weight distribution is

narrow enough to have a considerable overlap between the long chains belonging to each phase separated by the interface. These simulation results do not contradict with the recent experimental results.

Chapter 5

Summary

AMUSE is the project examining a prototype of virtual experiments by cooperating two or more simulation programs and a platform. By combining each simulation program on a platform, the practical simulations became possible to study various phenomena, which were difficult to deal with conventional approach.

1. The calculation of the elastic modulus and the analysis of the tensile behavior of semi-crystalline lamellae by COGNAC were attained by using the initial structure based on the mean field theory.
2. The elastic modulus of bulk materials which have multiphase structures can be predicted by using a part of MUFFIN, Elastica with introducing the three-dimensional morphology calculated by SUSHI.
3. The elastic modulus of bulk material in consideration of axial anisotropy can be predicted. Thereby, the orientation of crystallite can be dealt with.
4. The effective technique of generating the initial structure at the interface for MD simulation in COGNAC based on the morphology calculated from a mean field calculation done by SUSHI was developed. This zooming technique was applied to the analysis of peeling behavior of the interface of immiscible polymer blends.

Appendix A

Sample data

A.1 Lamella structures of semi-crystalline polymers

The sample files described in this section can be found in the following directory:

```
AMUSE/sample/lamella/sample1
                    /sample2
                    /sample3
```

The sample UDF files are listed below.

1. Minimization of the infinite chain of crystal polymer under the strain(/sample1)

   If you start InputUDF using COGNAC ,the infinite chains of pure crystal polymer are minimized by MM simulations under the the strain $\epsilon = \pm 0.001$ in z-axis direction of the cell. After calculation, you can get the stiffness matrix C_{ij} from the second derivatives of the difference of minimized energies δU before and after the deformations in following equation2.23. Elastic moduli are derivated from various components of the stiffness matrix C_{ij} (see sec.2.3.1.1).

   Table A.1: Sample: Minimization of the the infinite chain of crystal polymer under the strain.

Input UDF	Restart UDF Read_Set_of_MoleculesUDF	Output UDF
bs_crystal_def.udf	bs_crystal_mm_out.udf	bs_crystal_def_out.udf

2. Generating the lamella system of semi-crystalline polymer(/sample2)

   The lamella system of semi-crystalline polymer consisting 12000 beads $\times$ 4 chains is generated by a function of "lamella generator". Each bead is modeled by a bead-spring model. MD simulation with microcanonical ensemble (NVE) is carried out for 10 steps.
   Note: It is hopeful that MD simulation for long time is carried out, because of the elimination of anisotoropic pressure and the relaxation of the overall contortion of the system.

   Table A.2: Sample:Generating the lamella system of semi-crystalline polymer

Input UDF	Read_Set_of_MoleculesUDF	Output UDF
bs_lamella_in.udf	bs_lamella_in_str.udf	bs_lamella_in_out.udf

3. Elongation of the lamella system(/sample3)

Elongation of the lamella system in c-axis direction of crystalline phase is performed by MD simulation. The Poisson's ratio and strain rate $\dot{\epsilon}$ are set as 0.5 and $0.1\tau^{-1}$

Table A.3: sample: Elongation of the lamella system

Input UDF	Restart UDF Read_Set_of_MoleculesUDF	Output UDF
bs_lamella_elong.udf	bs_lamella_in_out.udf	bs_lamella_elong_out.udf

A.2 Bulk elasticity of polypropylene/elastomer blends

The sample files described in this section can be found in the following directory:

```
AMUSE/sample/elastic/crystalline
                    /other
                    /wi
```

The sample UDF files are listed below.

1. The sample files for the WI structure (`/wi`)
   The deformation of "shear", "uniaxial compression", "biaxial compression" to the direction of three axes of x, y and z are treated. The sample files are prepared to the nine deformation modes for the "WI structure" treated in the section "Prediction of the averaged elastic modulus" and shown in Table A.4. The "Log File" contain the standard output in the simulation and include the values required for the analysis.

Table A.4: Sample files for the WI structure (`/wi`)

Deformation Mode	Input UDF	Output UDF	Log File
shear to x axis	sushi1_1_in.udf	sushi1_1_out.udf	sushi1_1_result.txt
shear to y axis	sushi1_2_in.udf	sushi1_2_out.udf	sushi1_2_result.txt
shear to z axis	sushi1_3_in.udf	sushi1_3_out.udf	sushi1_3_result.txt
uniaxial compression to x axis	sushi1_4_in.udf	sushi1_4_out.udf	sushi1_4_result.txt
uniaxial compression to y axis	sushi1_5_in.udf	sushi1_5_out.udf	sushi1_5_result.txt
uniaxial compression to z axis	sushi1_6_in.udf	sushi1_6_out.udf	sushi1_6_result.txt
biaxial compression to x axis	sushi1_7_in.udf	sushi1_7_out.udf	sushi1_7_result.txt
biaxial compression to y axis	sushi1_8_in.udf	sushi1_8_out.udf	sushi1_8_result.txt
biaxial compression to z axis	sushi1_9_in.udf	sushi1_9_out.udf	sushi1_9_result.txt

2. The sample files of the shear to the x axis for the other structures (`/other` and `/crystalline`)
   Since the deformation modes for the other structures are the same as shown in Table A.4, the contents in the Input UDF files for these structures are almost the same other than the parts related to the structure (the number of components "`NUMBER_OF_COMPONENTS`" in "`parameter/physical_parameter`", the initialize condition "`INITIALIZE`" in "`dynamics_manager`" ...). Therefore, the only files of the shear to the x axis are prepared for these structures. The simulation can be examined by replacing the parameters related to the deformation (the deformation mode in "`region_condition`" and the boundary condition in "`parameter/mesh_parameter`") in these Input UDF files.

A.3 Interfacial strength of polypropylene/elastomer blends

The sample files described in this section can be found in the following directory:

Table A.5: Sample files for "Prediction of the Averaged Elastic Modulus" (`/other`)

Structure	Input UDF	Output UDF	Log File
NI structure	sushi2_in.udf	sushi2_out.udf	sushi2_result.txt
Dispersed structure	sphere_in.udf	sphere_out.udf	sphere_result.txt
Bicontinuous structure	cocon_in.udf	cocon_out.udf	cocon_result.txt

Table A.6: Sample files for "Calculation of the Elasticity of Crystalline Polymer" (`/crystalline`)

Structure	Input UDF	Output UDF	Log File
high orientation	micro_ori_in.udf	micro_ori_out.udf	micro_ori_result.txt
random	micro_ran_in.udf	micro_ran_out.udf	micro_ran_result.txt

```
AMUSE/sample/interface/morphology
                       /mol_structure
                       /peeling
```

The sample UDF files are listed below.

1. Calculation of segment density distribution (/morphology)
   You can obtain the spacial distribution of segments by using the following Input UDF files for SUSHI. The Output UDF files coresponding to each SUSHI calculation are prepared for generating an initial structure for the MD simulation.

Table A.7: Samples of SUSHI calculation for the DBMC method

Calculation model	Input UDF	Output UDF
monodisperseχ_{AB} 0.25	cognac100100_eq_uin.udf	cognac100100_eq_uot.udf
monodisperseχ_{AB} 0.1	cognac1001001_eq_uin.udf	cognac1001001_eq_uot.udf
polydisperseχ_{AB} 0.1	cognac555501_eq_uin.udf	cognac555501_eq_uot.udf

2. Calculation of initial structual data for COGNAC (/mol_structure)
   You can obtain the initial structure for MD simulation by using the following Input UDF files. Peeling behavior can be simulated by using the prepared Output UDF as initial structure input UDF for COGNAC.

Table A.8: Samples of COGNAC calclation for generating the initial structure for MD

Calculation model	Input UDF	Output UDF
Monodisperseχ_{AB} 0.25 SUSHIOutput UDF SILK UDF	blend_de100100_in.udf cognac100100_eq_uot.udf blend100_silk_str.udf	blend_de100100_out.udf
Monodisperse χ_{AB} 0.1 SUSHIOutput UDF SILK UDF	blend_de1001001_in.udf cognac1001001_eq_uot.udf blend100_silk_str.udf	blend_de1001001_out.udf
Polydisperse χ_{AB} 0.1 SUSIOutput UDF SILK UDF	blend_de555501_in.udf cognac555501_eq_uot.udf blend55550_silk_str.udf	blend_de555501_out.udf

3. Calculation of Stress-Strain behavior at the interface (/peeling)

Table A.9: Samples of COGNAC calculation for the peeling behavior

Calculation model	Input UDF	Output UDF
Monodisperseχ_{AB} 0.25 Initial structure for MD	blend_de100100md_in.udf blend_de100100_out.udf	blend_de100100md_out.udf
Monodisperseχ_{AB} 0.1 Initial structure for MD	blend_de10010001md_in.udf blend_de1001001_out.udf	blend_de1001001md_out.udf
Polydisperseχ_{AB} 0.1 Initial structure for MD	blend_de555501md_in.udf blend_de555501_out.udf	blend_de555501md_out.udf

References

1) Shoji, T., et al.: to be published.

2) DiMarzio, E. A. and Guttman, C. M.: *Polymer*, Vol. 21, p. 733 (1980).

3) Guttman, C. M., Dimarzio, E. A. and Hoffman, J. D.: *Polymer*, Vol. 22, p. 1466 (1981).

4) Doi, M. and Edwards, S. F. eds.: *The Theory of Polymer Dynamics*, Oxford University Press (1986).

5) Kremer, K. and Grest, G. S.: *J. Chem. Phys.*, Vol. 92, pp. 5057–5086 (1990).

6) Clarke, J. H. R. and Brown, D.: *Molecular Simulation*, Vol. 3, pp. 27–47 (1989).

7) Berendsen, H. J. C., Postma, J. P. M., Gunsteren, van W. F., Dinola, A. and Haak, J. R.: *J. Chem. Phys.*, Vol. 81, p. 3684 (1984).

8) Theodorou, D. N. and Suter, U. W.: *Macromolecules*, Vol. 19, pp. 139–154 (1986).

9) Nakamae, K., Nishino, T., Hata, K. and Matsumoto, T.: *Japanese Journal of Polym. Sci. Technol.*, Vol. 42, pp. 241–247 (1985).

10) Gautam, S., Balijepalli, S. and Rutledge, G. C.: *Macromolecules*, Vol. 33, p. 9136 (2000).

11) Brown, D. and Clarke, J. H. R.: *J. Chem. Phys.*, Vol. 84, pp. 2858–2865 (1986).

12) Barish, L.: *J. Appl. Polymer Sci.*, Vol. 6, p. 617 (1962).

13) Verhoogt, H., Langelaan, H. C., Dam, J. V. and Boer, de A. P.: *Polym. Eng. Sci.*, Vol. 33, pp. 754–763 (1994).

14) Machiels, A. G. C., Denys, K. F. J., Dam, J. V. and Boer, de A. P.: *Polym. Eng. Sci.*, Vol. 36, pp. 2451–2466 (1996).

15) Jordhamo, G. M., Manson, J. A. and Sperling, L. H.: *Polym. Eng. Sci.*, Vol. 26, pp. 517–524 (1986).

16) Mamat, A., Vu-Khanh, T., Cigana, P. and Favis, B. D.: *J. Polym. Sci. Part B, Polymer Physics*, Vol. 35, pp. 2583–2592 (1997).

17) Willemse, R. C., Boer, de A. P., Dam, J. V. and Gotsis, A. D.: *Polymer*, Vol. 39, pp. 5879–5887 (1998).

18) Favis, B. D. and Chalifoux, J. P.: *Polymer*, Vol. 29, pp. 1761–1767 (1988).

19) Veenstra, H., Dam, J. V. and Boer, de A. P.: *Polymer*, Vol. 40, pp. 1119–1130 (1999).

20) Veenstra, H., Lent, van B. J. J., Dam, van J. and Boer, de A. P.: *Polymer*, Vol. 40, pp. 6661–6672 (1999).

21) Veenstra, H., Verkooijen, P. C. J., Lent, van B. J. J., Dam, van J., Boer, de A. P. and Nijhof, A. P. H. J.: *Polymer*, Vol. 41, pp. 1817–1826 (2000).

22) Miles, I. S. and Zurek, A.: *Polym. Eng. Sci.*, Vol. 28, pp. 796–805 (1998).

23) Ho, R. M., Wu, C. H. and Su, A. C.: *Polym. Eng. Sci.*, Vol. 30, pp. 511–518 (1990).

24) Noda, M., et al.: to be published.

25) Ito, T.: *Polymer*, Vol. 23, pp. 1412–1434 (1982).

26) Davies, W. E. A.: *J. Phys. D, Appl. Phys.*, Vol. 4, pp. 1325–1339 (1971).

27) Nishiyama, Y. and Sperling, L. H.: *J. Appl. Polym. Sci.*, Vol. 32, pp. 5903–5915 (1986).

28) Ohlsson, B., Hassander, H. and Tornell, B.: *Polym. Eng. Sci.*, Vol. 36, pp. 501–510 (1996).

29) Aoyagi, T., et al.: submitted to the Conference Proceedings of ICAPP2001.

30) Grest, G. S., Lacasse, M.-D., Kremer, K. and Gupta, A. M.: *J. Chem. Phys.*, Vol. 105, p. 10583 (1996).

31) Aoyagi, T., Takimoto, J. and Doi, M.: *Polymer Prep. Jpn.*, Vol. 49, p. 2569 (2000).

32) Aoyagi, T., et al.: *Comp. Phys. Comm.* (in press.).

33) Fleer, G. J., et al. eds.: *Polymers at Interfaces*, Chapman and Hall, London (1993).

34) Matsen, M. W. and Bates, F. S.: *Macromolecules*, Vol. 29, p. 1091 (1996).

35) SUSHI (Simulation Utilities for Soft and Hard Interfaces) is a dynamic mean field program which has been developed in our group. See SUSHI user's manual for the details.

36) Flory, P. J. ed.: *Principles of Polymer Chemistry*, Cornell University Press, Ithaca, New York (1971).

37) Fayt, R., Jerome, R. and Tessie, P.: *J. Polym. Sci., Polym. Phys.*, Vol. 20, p. 2209 (1982).

38) Fayt, R., Jerome, R. and Tessie, P.: *J. Polym. Sci., Polym. Chem.*, Vol. 27, p. 2823 (1989).

39) Lindsey, C. R., Paul, D. R. and Barlow, J. W.: *J. Appl. Polym. Sci.*, Vol. 26, p. 1 (1981).

40) Chaffin, K. A., Bates, F. S., Brant, P. and Brown, G. M.: *J. Polym. Sci., Polym. Phys.*, Vol. 38, p. 108 (2000).

41) Yokomizo, K., et al.: submitted to the Conference Proceedings of ICAPP2001.

42) Broseta, D., Fredrickson, G. H., Helfand, E. and Leibler, L.: *Macromolecules*, Vol. 23, p. 132 (1990).

43) Chaffin, K. A., Knutsen, J. S., Brant, P. and Bates, F. S.: *Science*, Vol. 288, p. 2187 (2000).